DRAFT

MECHANICAL PROPERTIES OF NTS TUFF FOR EVALUATION OF MINEBACK TESTS

by

Chapman Young
Thomas L. Blanton
Nancy C. Patti

TASK REPORT

September 12, 1980

Prepared for

Eastern Gas Shales Project
Morgantown Energy Technology Center
Collins Ferry Road
Morgantown, West Virginia 26505

Contract No. DE-AT21-78MC08216
Task Order No. 21

Prepared by

Science Applications, Inc.
P.O. Box 1173
Steamboat Springs, Colorado 80477

Executive Summary

A major component of the Eastern Gas Shales Project being conducted by the Morgantown Energy Technology Center is the development and evaluation of new and refined stimulation techniques which might be suitable for stimulating Devonian shale wells. As part of the EGSP stimulation development program, several dynamic stimulation techniques employing combinations of explosives and/or propellants are being evaluated through a series of mineback experiments at the Nevada Test Site (NTS). As the experiments being conducted at the NTS are being carried out in one of the volcanic tuff formations found at the site, a complete evaluation of the field-test results will require an adequate knowledge of the mechanical properties of the tuff rock. Several of the research firms and agencies participating in the EGSP have or will conduct calculations to simulate certain aspects of the stimulation treatments being evaluated at the NTS. Science Applications, as one of the firms conducting these evaluations, is employing explicit finite difference programs to simulate in both 1-D and 2-D calculations the various stimulation treatments being evaluated. The proper execution of these calculations requires that suitable material properties be available on the NTS tuff.

As the existing data base on the mechanical properties of NTS tuff is limited, it has been necessary to carefully review existing data on the tuff and to generate additional data as required. The review, experiments and evaluation which have been conducted have resulted in the following principle conclusions:

- The yield surface defined by triaxial experiments for the G-Tunnel tuff is significantly lower from that defined for other tuff beds at the NTS.
- Direct-pull tensile strength data obtained within this testing program compares favorably with that obtained by Sandia on the same tuff bed.
- The tensile strength of this rock, although quite variable, is moderately low with values on the order of 1.6 MPa being typical.

- Fracture energy values measured for the G-Tunnel tuff, averaging 9 J/m^2, are quite low as compared to most other rock types, and are a measure of the very fragile nature of the rock.
- Dynamic experiments employing modified Split-Hopkinson-Bar techniques, indicate that the dynamic strength of this rock is only slightly higher than the static strength.
- The dynamic yield data suggests that quasi-statically determined yield surfaces would be suitable for inclusion in calculations to evaluate various dynamic stimulation treatments in the NTS tuff.
- The dynamic data reveal that the sample deformation is characterized by an initial compaction followed by sample bulking (dilatancy) associated with failure.
- As the relationships between compaction, yielding and mode of failure will depend strongly upon pore-pressure effects, as controlled by the degree of sample saturation, additional experimental data will be required to completely describe the importance of saturation.

MATERIAL PROPERTIES OF NEVADA TEST SITE TUFF

Introduction

Dynamic stimulation treatments are being experimentally evaluated at the Nevada Test Site (NTS) where a mineback allows direct observation of the results of the experiments. Five different treatments have been performed, as follows:

Dynafrac - a fluid-decoupled explosive,
Augmented Dynafrac - a fluid-decoupled explosive with a propellant booster,
Kinefrac - a small diameter propellant charge with a pressurized water pad,
Multiple Kinefrac - three successive Kinefracs,
High-Energy Gas Frac - a full diameter charge of a progressively burning propellant.

The object in each case is to produce multiple fractures that remain connected to the wellbore after the treatment. Evaluation of the success or failure of these treatments and their potential for use in other rocks is heavily dependent on a knowledge of the material properties at in situ conditions. The rock at the NTS is an ash-fall tuff whose properties differ markedly from those of most reservoir rocks. To assist in the analysis of the experiments, computer codes are being used to perform parameter sensitivity studies. These codes require specific material property data as input as well as information on the variability of these properties both within the tuff and between the tuff and other rocks being considered. An example of such a code is STEALTH/CAVS being used by Science Applications, Inc. (SAI) to model the NTS experiments. Material properties required by the code are: (1) mass density, (2) elastic constants, (3) tensile strength, and (4) yield envelope. Information on compaction and anisotropic behavior can also be used in the code for more refined models.

The purpose of this report is to collect as much material property data as possible to form a data base for the analysis and evaluation

discussed above. At present, data being used to characterize the tuff are based on static tests run on samples of rock from locations other than the actual site of the stimulation experiments.[1,2,3,4] These tests are inadequate in two respects. First, they are not site-specific, and what few tests have been run suggest that the tuff can be quite heterogeneous with respect to some material properties such as tensile strength.[5] In order to get more site-specific data, additional static tests were run by Atkinson-Noland & Associates (A-N) on samples from G-Tunnel where the experiments are being run and from a tunnel adjacent to G-Tunnel (see Appendix A). Second, the static tests are not adequate for evaluating the effect of the dynamic loads produced by these types of stimulation treatments. To fill this gap in the data base, SAI has run Split-Hopkinson-Bar (SHB) experiments to determine the dynamic mechanical properties of the tuff.

In Situ Conditions

The stimulation treatments were run in horizontal, 15 cm holes drilled 12.2 m deep from the tunnel. The overburden stress in the vicinity of the tunnel is 8.6 MPa. The minimum horizontal principal stress is 5.4 MPa and is oriented at 15° to the drilled holes. The maximum horizontal principal stress is 10.3 MPa.

In situ, a significant portion of the bulk material is water. The tuff has a porosity of about 40% and it is water-saturated. The mass density is only 1.8 gm/cm^3. Even though the porosity is high the pores are not well connected. The permeability ranges from 0.01 md to 0.80 md. Under dynamic loading conditions, this low permeability could cause pore pressures to build up thus reducing the effective stresses. This must be kept in mind in analyzing the mechanical data presented.

Static Tests

Elastic properties. The two sources for static elastic properties are Sandia Laboratories and the work done by Atkinson-Noland (A-N) whose work is presented in Appendix A. Values for Young's modulus published by Sandia are 4 GPa (600 ksi)[2,3] and 5 GPa (725 ksi)[4]. Subsequent tests in which a special effort was made to keep the rock water-saturated gave a lower average Young's modulus - 2.76 GPa (400 ksi)[5]. However, it was emphasized in

personal communication[5] that the number of tests was too small to form a basis for any conclusions about the effects of water-saturation. It was felt that the variation in Young's modulus may be due more to the heterogeneity of the rock than to the effects of water.

The values for Young's modulus obtained by A-N (see Table 1) are generally lower than those obtained by Sandia. The average from 25 tests is 2.62 MPa (380 ksi) ± 0.80 MPa (117 ksi). The degree of heterogeneity is reflected in two ways: first by the standard deviations and second by comparing averages from two different tunnels (Series I and Series II). The standard deviations are relatively large, which supports Sandia's feelings about the heterogeneity of the rock. These standard deviations reflect variations over a distance of about 3 m, which is the length of core from which samples in a given group were taken. Comparing the values for Series I and Series II in Table 1 gives an idea of the heterogeneity on a scale of about 30 m (distance between tunnels. Again the rock appears to be heterogeneous, but less than it was on the smaller scale.

In analyzing and modeling the static elastic behavior of the rock, it is recommended that A-N's overall average of 2.62 GPa be used for Young's modulus. This average is based on 25 tests all run under the same testing procedures and in which a special effort was made to keep the rock water-saturated.

A-N's tests also examined the dependence of elastic properties on confining pressure and direction of loading. Table 1 shows no clear trend for variation of Young's modulus with confining pressure. This conclusion is supported by the plot of Young's modulus vs. confining pressure in Figure 32 of Appendix A. Table III of Appendix A (page 15) shows only a small variation of Young's modulus with direction.

The other elastic constant, Poisson's ratio, also seems to vary by a considerable amount. The value published by Sandia is 0.2[3]. The average value measured by A-N is 0.38 ± 0.16. Four of the values were greater than 0.5, suggesting some inelastic dilatant behavior at relatively low stresses.

Tensile strength. Tensile strengths have been measured in three labs: Sandia's, SAI's, and A-N's. Values for tensile strength published

Table 1. Young's moduli for NTS tuff from different locations (Series I adjacent to G-Tunnel, Series II in G-Tunnel). Numbers are given as follows: GPa(ksi) ± standard deviation (number of samples).

	Series		
	I	II	I & II
Unconfined	1.79 (260) ±0.28 (40) (2)	2.60 (377) ±0.53 (76) (7)	2.42 (351) ±0.59 (85) (9)
Confined	3.12 (452) ±0.70 (101) (8)	2.35 (344) ±0.95 (138) (8)	2.74 (397) ±0.90 (131) (16)
Unconfined & Confined	2.85 (413) ±0.84 (122) (10)	2.47 (358) ±0.77 (111) (15)	2.62 (380) ±0.80 (117) (25)

by Sandia are 2.76 MPa (400 psi)[3] and 0.70 MPa (100 psi)[4]. A completely water-saturated sample showed a tensile strength of only 0.32 MPa (47 psi)[5]. Again the feeling was that this variation may reflect overall rock heterogeneity rather than the effects of water. The tests were direct-pull tests on 6 inch diameter samples. Direct-pull tests on 1.5 inch diameter samples performed by SAI gave a value of 0.84 MPa (122 psi). Pinch tests performed by SAI gave an indirect tensile strength of 1.84 MPa (268 psi). Another indirect measure of tensile strength was obtained from Brazil tests run by A-N. The average for 24 tests was 1.58 MPa (229 psi). Tests on samples of different orientation showed no significant variation of tensile strength with direction (see page 11 of Appendix A).

In summary, both the highest and lowest value for tensile strength were given by Sandia. The range from 2.76 MPa to 0.32 MPa is not unusual for tensile strengths. For analysis and modeling purposes, the value of 1.58 MPa from A-N's tests is probably best since it is based on a large number of tests and falls near the middle of the range of values measured in other laboratories.

Compressive strength. Uniaxial compressive strengths are given by three sources. Sandia gives values of 34.5 MPa (5000 psi)[2,3] and 30 MPa (4350 psi).[4] SAI obtained an average value of 12.1 MPa (1760 psi), which compares favorably with the value obtained by A-N of 13.6 MPa (1975 psi). The values given by Sandia seem high compared to those obtained in other labs.

The results of differential compression tests run by A-N are used to generate a yield envelope. These data are summarized in Table 2. A least-squares parabala fit to this data gives:

$$Y = 14.56 +).4847P - 0.005826\ P^2$$

where

Y = differential stress (MPa)

P = confining pressure (MPa)

Figure 1 compares this yield envelope with one based on tests run by Terra Tek.[1]

Information on compaction behavior can be obtained from the hydrostatic compression tests in Appendix A, Figures 2-15. The curves in

Table 2. Results of differential compression tests on NTS tuff.

Series	Test No.	Group	Confining Pressure P (MPa)	Differential Stress at Failure Y (MPa)
I	3	A	0	14.7
I	4	A	0	15.7
II	11	A	0	13.8
II	12	A	0	10.3
I	5	B	17.2	26.1
I	6	B	17.2	21.0
II	13	B	17.2	30.8
II	14	B	17.2	18.1
I	7	C	34.5	28.5
I	8	C	34.5	20.3
II	15	C	34.5	18.8
II	16	C	34.5	18.5
I	9	D	51.7	31.0
I	10	D	51.7	32.6
II	17	D	51.7	18.2
II	20	D	51.7	18.2

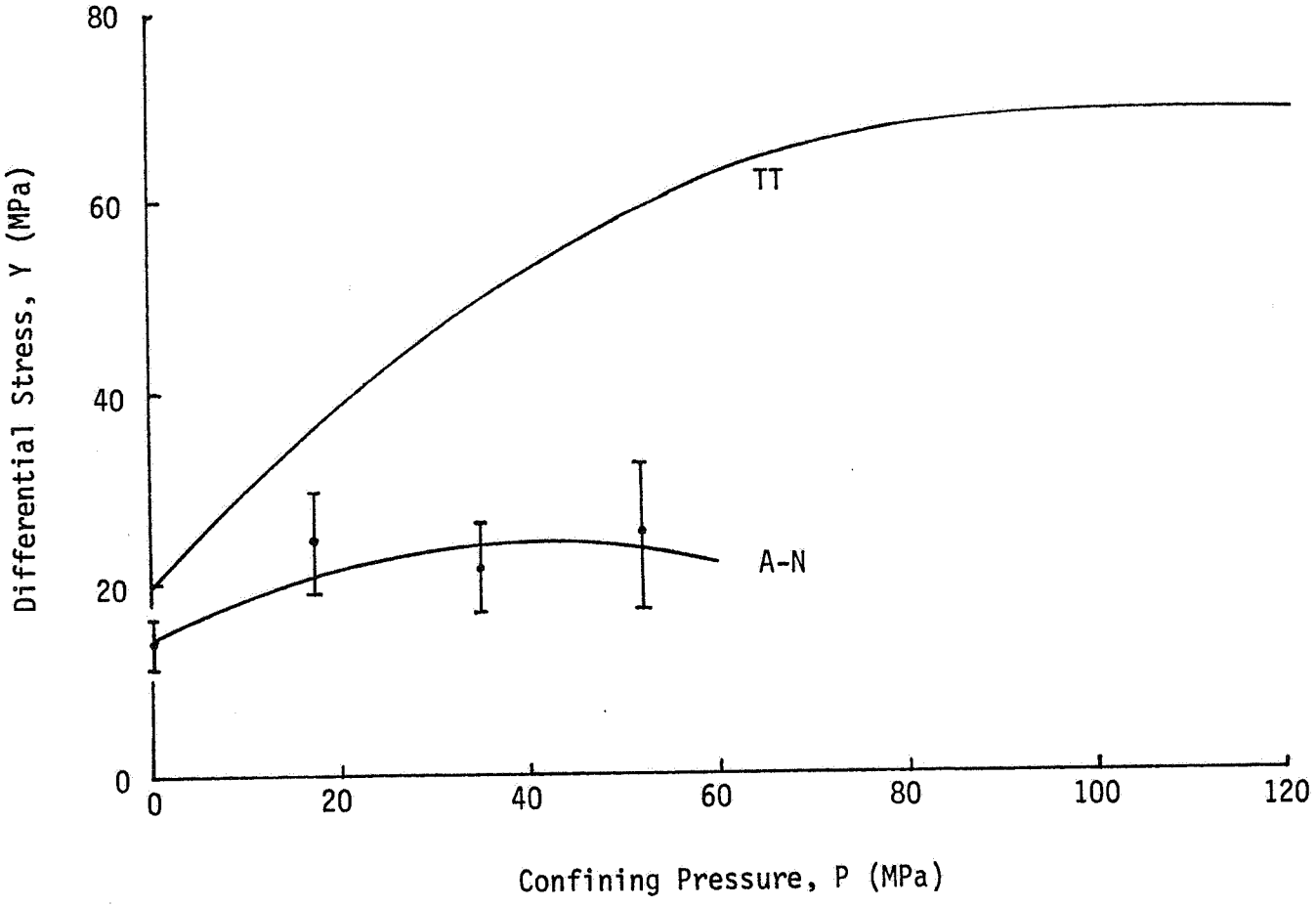

Figure 1. Yield envelopes for NTS tuff based on tests run by Atkinson-Noland (A-N) and Terra Tek (TT).

these figures may be characterized in three stages. In the first stage the curve has a relatively low slope. This is due to the closing of microflaws and is typical behavior for most rocks at low stresses. Between 3 and 15 MPa the curves steepen and become linear. In this stage the rock is behaving elastically and the slope of the curve here is the bulk modulus. An average bulk modulus for these curves is 2.09 GPa. Between 30 and 50 MPa the slope begins to decrease. This probably represents the onset of pore collapse.

Fracture mechanics. Measures of strength from the point of view of fracture mechanics were obtained in two labs. Sandia published values for fracture toughness of 495 $kPa\sqrt{m}$[2,3] and 400 $kPa\sqrt{m}$[4]. SAI obtained an average fracture energy of 9.16 J/m^2. The fracture toughness values can be converted to fracture energies according to the following equation:

$$G = K^2 (1-\nu^2)/E$$

where

G = fracture energy
K = fracture toughness
ν = Poisson's ratio
E = Young's modulus

Using A-N's values of E = 2.62 GPa and ν = 0.38 and Sandia's value of 400 $kPa\sqrt{m}$ to calculate a fracture toughness gives 52.3 J/m^2 which is much higher than the SAI value. It should be noted that Sandia's values for strength, both tensile and compressive, were higher than those obtained by SAI and A-N.

Dynamic Tests

While the quasi-static triaxial experiments discussed above can provide well-defined yield surfaces and compaction behavior for the NTS tuff, the experiments do not provide any information on degree or importance of dynamic-rate effects. It was considered essential to conduct some form of dynamic experiment so as to evaluate the potential importance of rate effects in NTS tuff yielding and compaction. If the rate effects are minimal, then the yield surface and compaction equation-of-state derived from static experiments may be utilized directly in calculations of dynamic phenomena. If dynamic-rate effects are found to be important then the appropriate modifications could be made to the descriptions of yield and compaction derived from the static experiments. As the maximum loading rates to be experienced in the NTS mineback experiments would be comparable to those realized in Split-Hopkinson-Bar (SHB) experiments, (10^2 to 10^3/sec), it was decided to use a modified SHB technique to evaluate dynamic-rate effects in NTS tuff.

The dynamic experiments were conducted in collaboration with the Geotechnical Laboratory of Colorado State University. This laboratory has an operational modified SHB apparatus designed so that electromagnetic in-material partical-velocity measurements may be made. This apparatus which is described in detail in Appendix B comprises the two traditional suspended bars between which the sample to be tested is placed. An air-driven canon is utilized to accelerate an impact piston against the first (driver) bar. This impact generates a bar stress wave which propagates down the driver bar arriving at the sample. Depending on the sample's impedance and mechanical response, this incident stress wave is partially transmitted through the sample and partially reflected back into the driver bar. By means of strain gages placed upon the two bars, the incident stress wave, the reflected stress wave and the stress wave transmitted through the sample may all be independently measured. Traditionally, an analysis of these waves is made so as to deduce dynamic strength characteristics for the sample material. As samples in SHB experiments typically deform heterogeneously rather than homogeneously, it is valuable to have information on the deformational behavior within the sample propper. Without specific information on heterogeneous sample deformation, sample response can only be inferred as if the sample acted as a homogeneous coupling

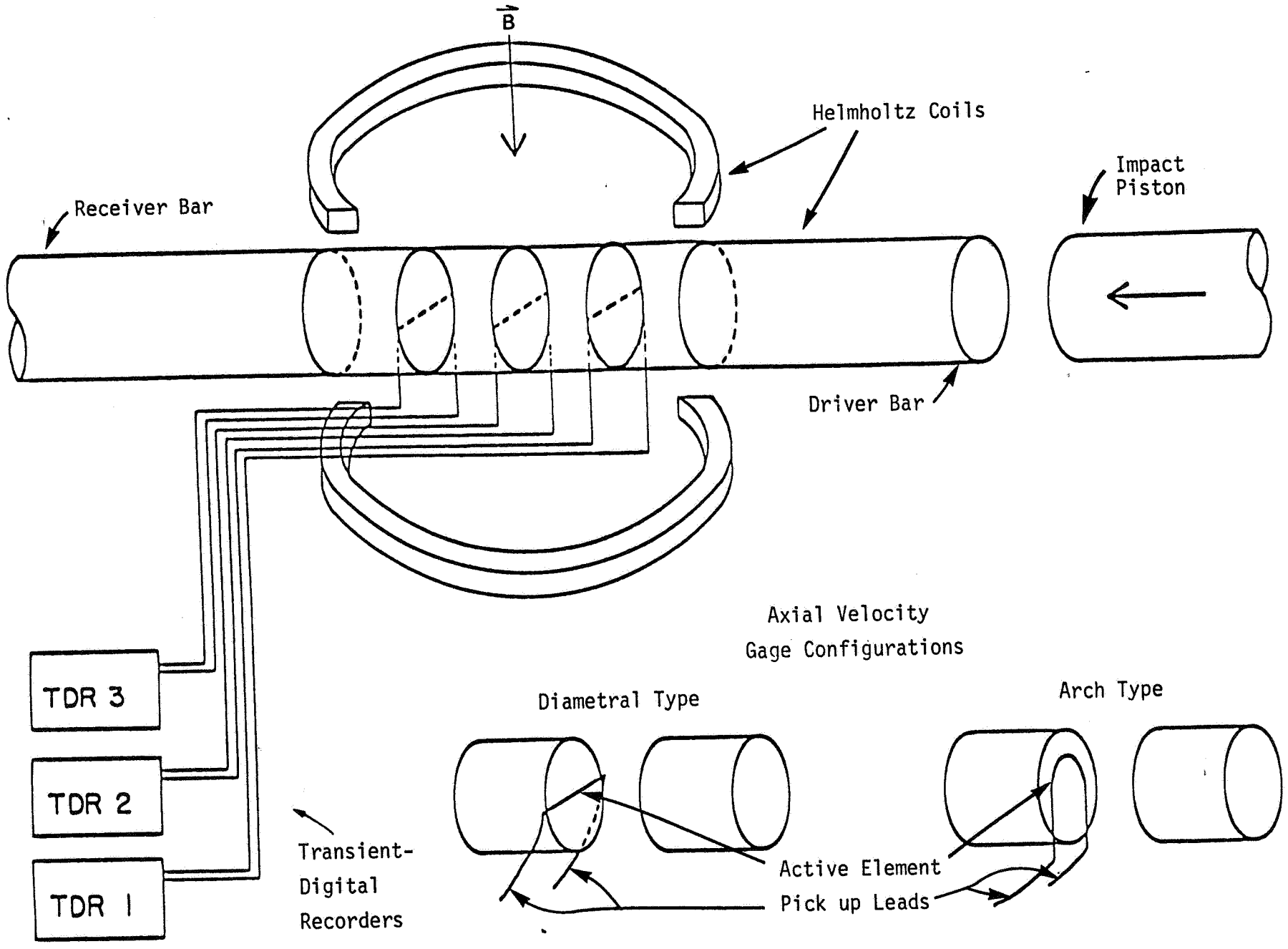

Figure 2. Schematic view of axial NTS tuff sample shown with magnetic field generated perpendicular to sample axis.

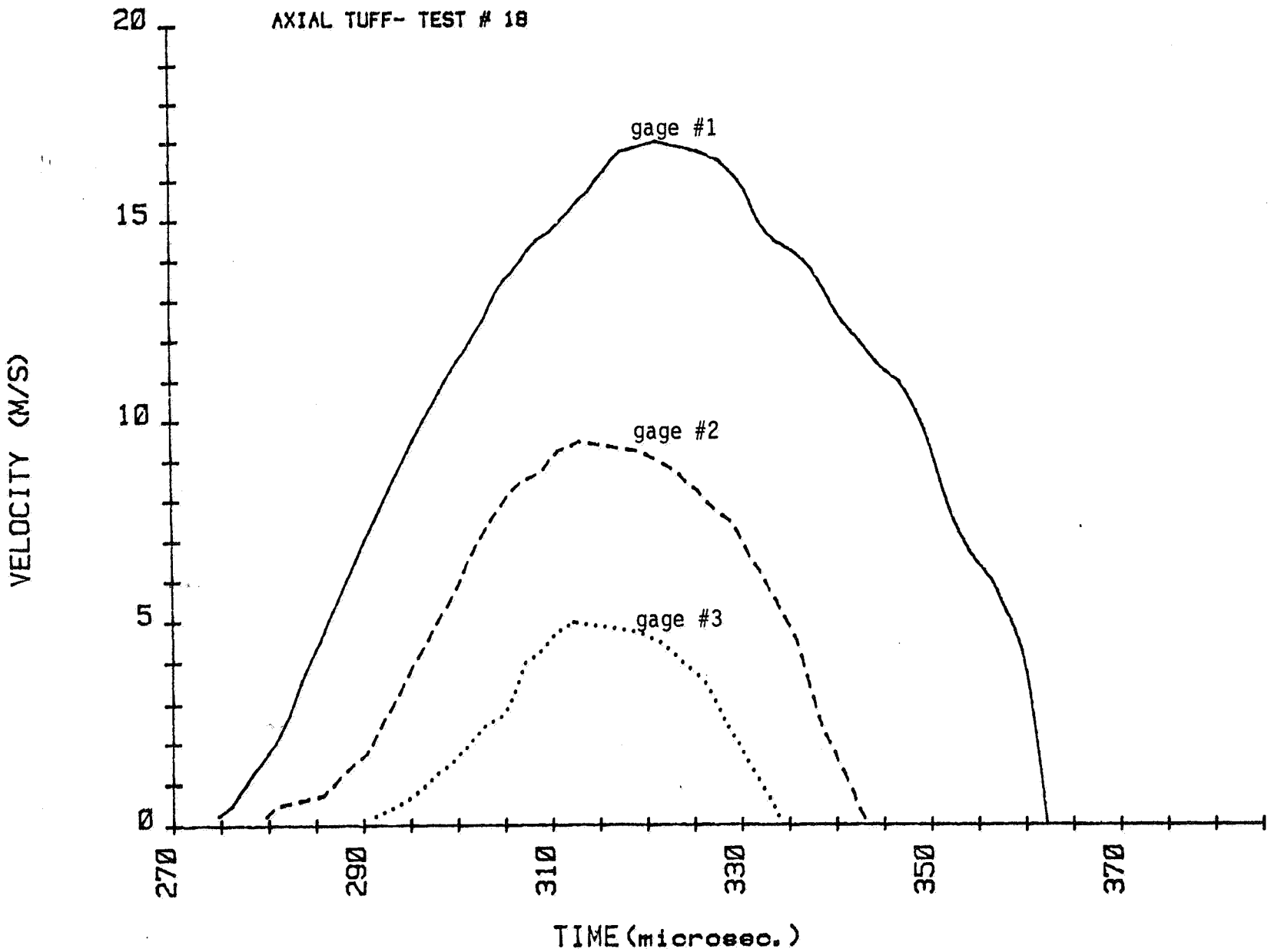

Figure 3. Partical velocity vs. time gage records for an axial SHB test with an impact piston velocity of 30 M/S.

amplitude of applied stress wave.

A second configuration of electromagnetic gage was utilized to measure radial deformation of the sample during failure. Gages designed to make radial partical-velocity measurements require that the Helmholtz-coil-generated magnetic field be aligned along the axis of the sample as illustrated in Figure 4. The electromagnetic gage loops for these measurements comprise concentric loops of conducting wire with pick-up leads located along radii of the sample, as illustrated in Figure 4. As a sample is axially shortened in the modified SHB apparatus, the sample undergoes outward radial displacements, both on the sample surface and within the sample. The concentric gage loops provided a direct measure of the radial velocities associated with the elastic and plastic deformation of the samples. A typical set of radial partical velocity measurements obtained on a sample loaded by an impact piston at 30 meters-per-second is illustrated in Figure 5. The curves shown in Figure 5 have been corrected for active gage length so that actual partical velocities as a function of time at different radii are given. Also, these curves have been smoother by using a three-point running average to numerically filter out some of the high-frequency noise characteristic of raw gage records. The most characteristic feature of these radial-velocity gage records is the marked decay radially inward of partical-velocity amplitude. In previous experiments conducted by Colorado State University on limestone and granite rock samples, an even stronger variation in radial velocity as a function of radius was noted. For these rocks, the strong divergence of radial velocities could only be explained by a large increase in sample cross-sectional area partially associated with dilatancy during sample failure. As will be discussed in more detail later, the NTS tuff samples displayed an early-time compaction behavior followed by late-time dilatancy. It is important to note that the accelerations necessary to achieve the velocities illustrated in Figure 5 can only be effected if appropriate radial-driving forces or stresses are present. These radial stresses will act as a confining stress or pressure on the material inside the material being accelerated. A knowledge of the radial velocities and accelerations as a function of radii as obtained with the concentric electromagnetic gage loops enables the accelerations to be integrated so that the radial stress acting within the sample as a function of radii may be calculated. For

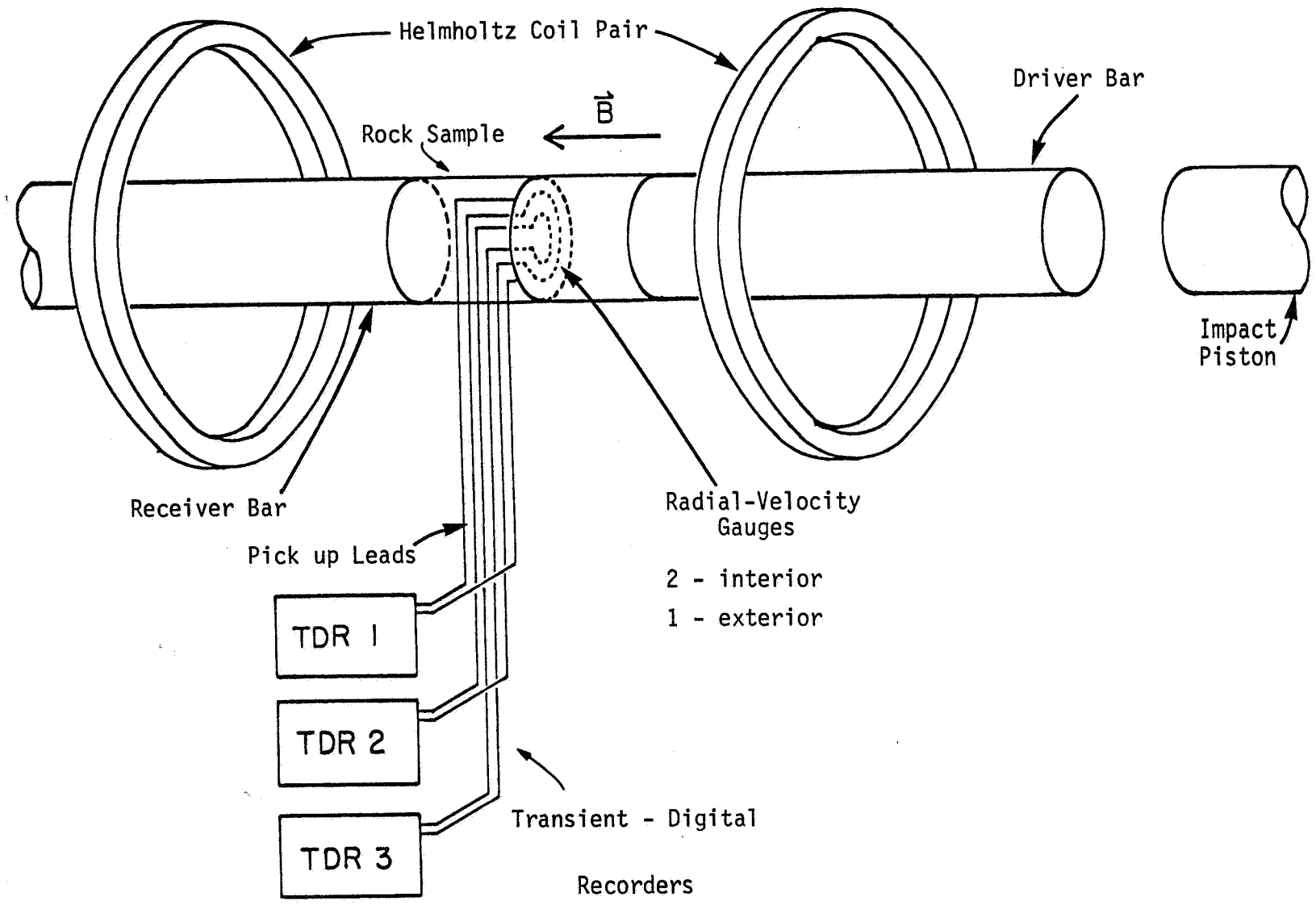

Figure 4. Schematic view of radial NTS tuff sample shown with magnetic field generated parallel to sample axis.

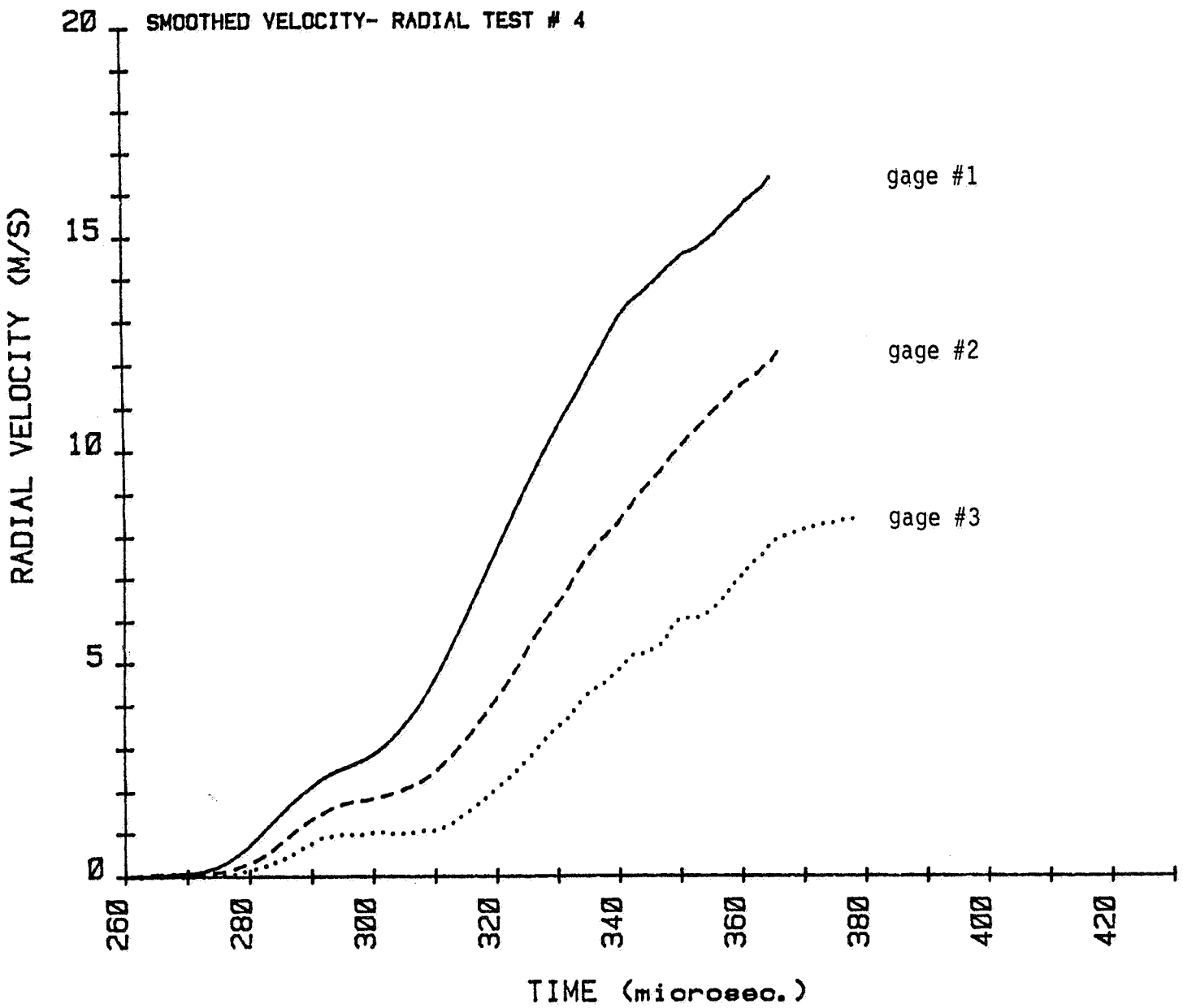

Figure 5. Partical velocity vs. time gage records for a radial SHB test with an impact piston velocity of 30 M/S.

brittle rock, undergoing strongly dilatant behavior, these radial stresses may be on the order of one kilobar. For the NTS tuff samples, in which dilatancy is much less pronounced, the peak radial stresses were less than 5 MPa (750 psi).

With the axial velocity data obtained from three different positions within the SHB sample, such as illustrated in Figure 3, it is possible to calculate the average axial stress-strain relationships existing in the sample during its dynamic deformation. Calculation of the dynamic stress-strain relationships involves integrating the velocity curves at any of the gage positions with an appropriate description of the phase velocity for wave propagation along the sample. As discussed by Fowles & Williams[6] two characteristic phase velocities are defined for one dimensional wave propagation. These two phase velocities are defined as:

$$C_p = \left(\frac{\partial h}{\partial t}\right)_p,$$

$$C_u = \left(\frac{\partial h}{\partial t}\right)_u,$$

where h is the Lagrangian coordinate position, t is time and p and u indicate the value of the derivative at constant p-wave stress and particle velocity respectively.

These phase velocities represent the speed at which stress or particle velocity information is propagated along the sample. For a steady wave C_p and C_u would be equal and would equal the classical compressive wave velocity for the material. A plot of wave amplitude arrival time vs. gage position, as illustrated in Figure 6, provides both a "contour map" of the spacial and temporal distributions of particle velocities in the sample and a visual representation of the phase velocities, C_u. The phase velocities are simply the slopes in the time vs. gage-position plane of lines connecting points of equal particle velocity. As indicated in Figure 6, both positive and negative phase velocities are indicated for the rising and falling portions of the particle velocity gage records, respectively. When equal particle velocities were measured at three gage positions, a parabolic fit was utilized to determine the phase velocity relationships along the sample. When only two gages measured a given particle velocity a linear relationship was utilized as illustrated in Figure 6. The axial stresses acting within

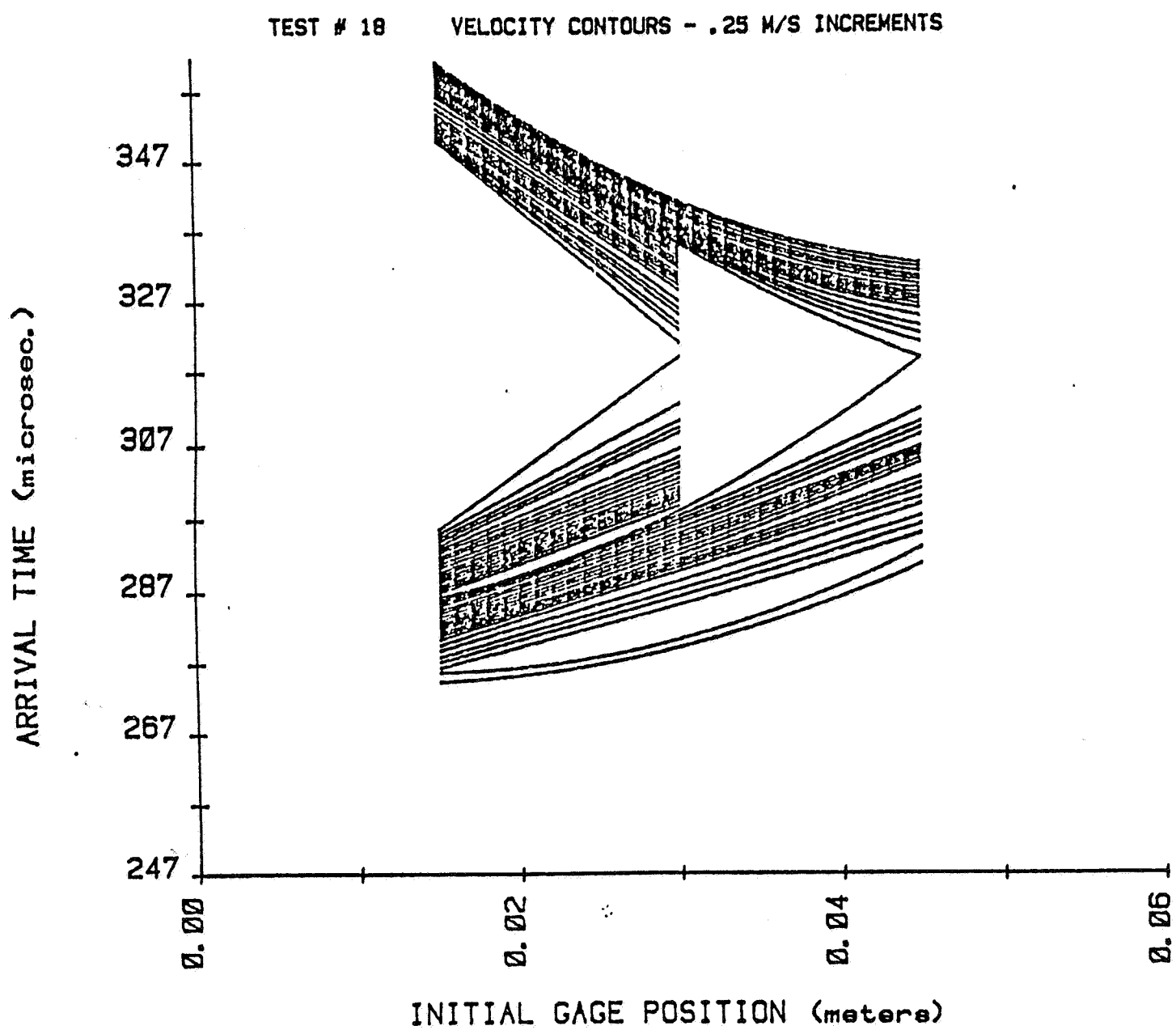

Figure 6. Wave amplitude arrival time vs. gage position

the sample during deformation were obtained by numerically integrating the equation:

$$\sigma = \rho_o \, C_p \frac{\partial u}{\partial t} dt,$$

which describes the relationship between stress phase velocity, particle velocity and density. A similar numerical integration of the equation:

$$\varepsilon = \frac{1}{C_u} \frac{\partial u}{\partial t} \, dt,$$

describing the relation between strain and particle and phase velocity, yields a description of axial strain vs. time at the various gage positions. As phase velocities are not defined for the higher velocity portions of the first gage, only the second and third gage records may be fully integrated utilizing the two relations given above. The axial-stress strain curves obtained from the velocity data illustrated in Figure 3 and the phase relations calculated from Figure 6 are given in Figure 7. The stress strain curve for the middle gage reveals a characteristic knee occurring at 23 MPa and 0.8% strain. This knee is associated with the onset of large-scale yielding of the sample. The secant slope of the middle gage stress strain record of 3.2 GPa (464 ksi) is slightly higher than the elastic moduli determined from the triaxial tests performed by Sandia and Atkinson-Noland on saturated samples. The 23 MPa strength indicated by the change in the slope of the stress strain curve is significantly higher than the unconfined compressive strength determined from static tests. Assuming that a 5 MPa confining stress is effective due to the radial inertia effects discussed above, an 18 MPa stress difference is indicated which compares closely with the 17 MPa stress difference obtained by Atkinson-Noland at a 5 MPa confining stress. Certainly, no major strain rate dependency is observed for the yield behavior of the NTS tuff. Integration of the third particle velocity gage indicates a continuation of elastic loading of the sample even after the peak particle velocity has been obtained as illustrated in Figure 7.

By combining the data obtained from comparable experiments with axial and radial partical-velocity gages, it is possible to obtain the volume variation of various regions of the sample as a function of time. A volume vs. time curve calculated from comparable radial and axial velocity experiments is illustrated in Figure 8. The characteristic feature of this curve is the early-time compaction followed by later-time dilatancy. The

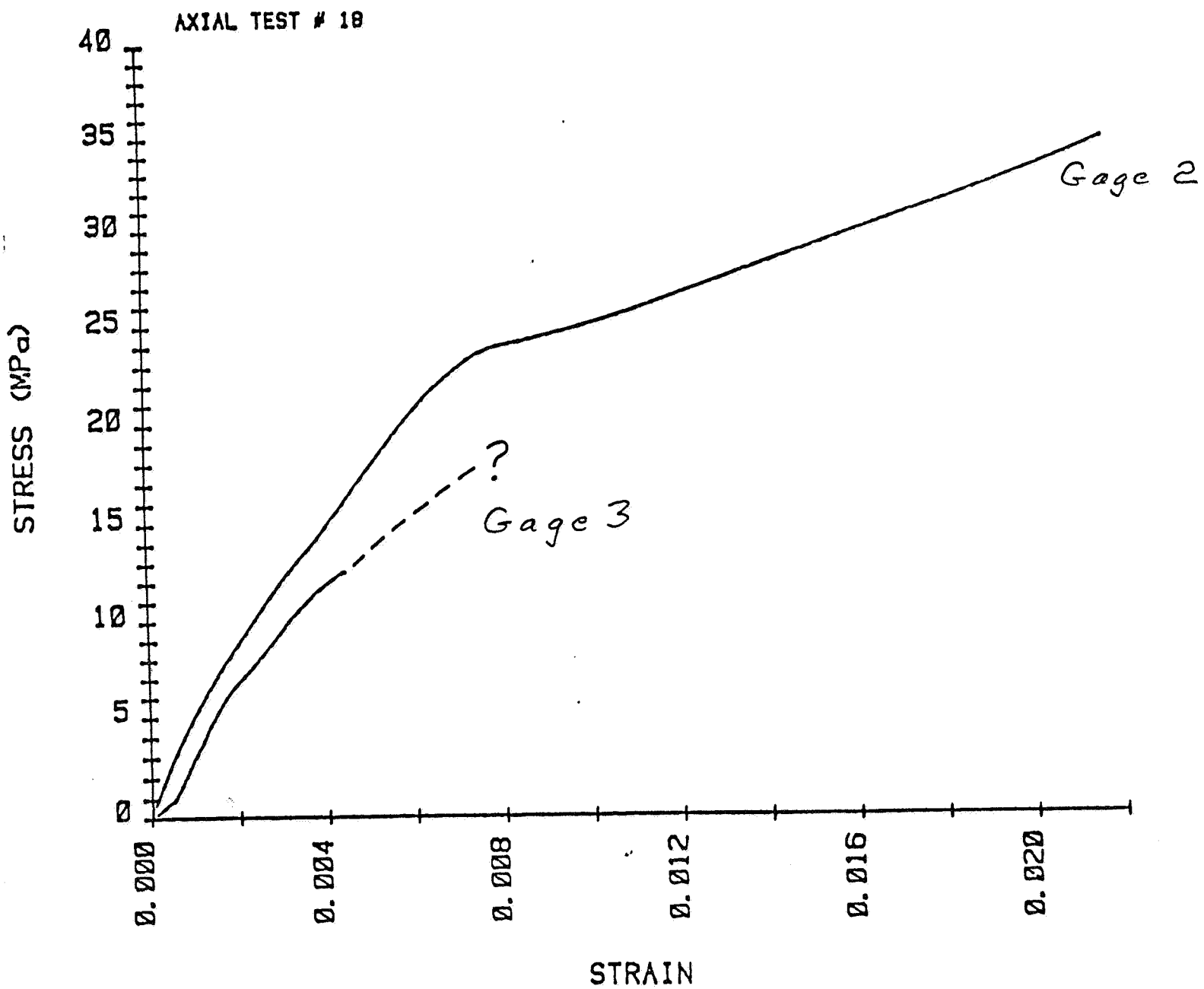

Figure 7. Calculated axial stress vs. strain relationship.

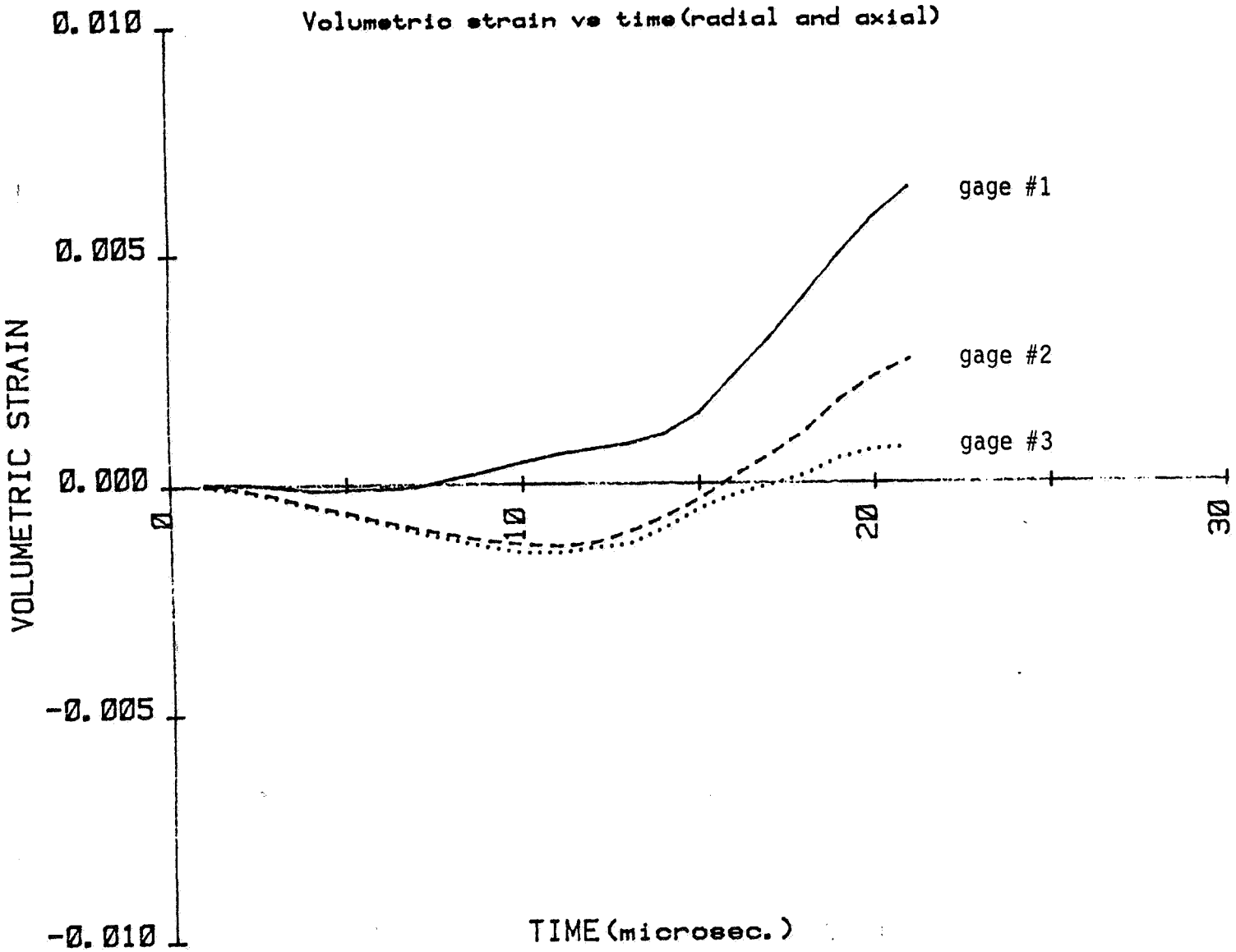

Figure 8. Volumetric strain vs. time calculated from comparable axial and radial tests.

transition from compaction to dilatant behavior is believed to be associated with the onset of large-scale sample failure. Prior to the onset of failure, the large porosity of the rock allows fairly significant compaction to occur due to the dominantly compressive stresses acting. Once failure begins to occur on a broad scale, however, the sample undergoes rapidly accelerating radial strains which effect a net increase in sample volume or characteristic dilatant behavior. As the samples were completely saturated prior to testing, any compaction would lead to the pressurization of the pore fluid and a consequent pore-pressure effect on axial failure. It was not possible to analyze in detail the role of pore-pressure effects in the experiments conducted.

The dynamic data obtained from the modified Split-Hopkinson-Bar experiments indicate that the dynamic strength of the G-Tunnel tuff is not significantly greater than the statically determined values. The dynamic experiments also reveal an initial compaction of the rock followed by dilatant behavior associated with overall sample failure. As this transition from compaction to dilatant behavior is probably controlled by pore-pressure effects occurring in the fully saturated rock additional experiments would be required to determine dynamic yield behavior of partially saturated tuff.

REFERENCES

1. Butters, S.W., Jones, A.H., and Dropek, R.K., "Material Properties of Nevada Test Site Tuff and Grout - with Emphasis on the Mighty Epic Event," November 1976, DNA4235F, prepared by Terra Tek, Inc.

2. Warpinski, N.R., Schmidt, R.A., Walling, H.C., Cooper, P.W., and Finley, S.J., "High Energy Gas Frac," SAND78-2342, December 1978.

3. Schmidt, R.A., Warpinski, N.R., and Northrop, D.A., "In Situ Testing of Well-Shooting Concepts," Proc. Third Eastern Gas Shales Symposium, 1979, 293-302.

4. Schmidt, R.A., Warpinski, N.R., and Cooper, P.W., "In Situ Evaluation of Several Tailored-Pulse Well-Shooting Concepts," Proc. First Annual Symposium on Unconventional Gas Recovery, 1980, 105-116.

5. Schmidt, R.A., personal communication, November 1979.

Preface

This report presents results obtained from a laboratory testing program conducted on tuff samples from the Nevada Test Site. This work was authorized by Science Applications, Inc. (SAI) Purchase Order No. 67194 dated February 26, 1980 and Purchase Order No. 67195 dated March 21, 1980. Tom Blanton, SAI, Fort Collins, Colorado served as SAI's technical representative.

This work was conducted under Atkinson-Noland & Associates, Inc. Project No. 7931 and was directed by Dr. R.H.Atkinson. Laboratory facilites of the University of Colorado, Boulder were utilized for the experimental work.

STRENGTH AND DEFORMATIONAL CHARACTERISTICS OF NEVADA TEST SITE TUFF

Introduction

A laboratory testing program was conducted to determine both strength and deformational characteristics of ash fall tuff samples obtained from the Nevada Test Site. This report discusses specimen preparation methods, test equipment, test procedures and presents results of the testing program.

Specimen Storage and Preparation

Tuff samples were delivered to the laboratory in two lots, the first on December 17, 1979 and the second on March 7, 1980. The two groups of samples referred to in this report as Series I and Series II respectively, were slightly different in visual appearance. The Series I tuff had a reddish color with inclusions of ash ranging in size up to 1 cm. The Series II material, which was obtained from Sandia Labs, had a pink color and a smaller, more uniform grain size.

The samples, which were in the form of 6 inch diameter core lengths, were stored under water from the time of delivery until the specimens were cored. The specimens for the hydrostatic and triaxial tests were cored from the 6 inch cores with the test specimen core axis parallel to the 6 inch core axis

The axial and lateral deformation tranducers and the load cell are full bridge strain gage circuits which are powered by a 10.000 VDC HP power supply. The output signals are plotted on an Esterline-Angus X-Y-Y' recorder.

Calibration

All transducers were calibrated at the beginning and at the end of the testing program. The load cell was calibrated using a standard laboratory testing machine which has a calibration traceable to the Bureau of Standards. The axial cantilevers were calibrated using a micrometer to supply a known deflection. The lateral cantilevers were calibrated in place using an expanding mandrel tool which permits deforming the inside of the membrane radially outwards by known amounts.

Under increasing hydrostatic loading, the increase in the internal confining pressure produces a deformation of the cell body which results in deformation of the lateral cantilevers which are mounted to the end cap of the cell. This deformation under increasing confining cell pressure was determined by subjecting a steel specimen to a hydrostatic loading cycle. The measured lateral response, when corrected for the steel specimen deformation, yielded a calibration curve for cell deformation due to changing internal pressure.

Test Procedure (Triaxial Tests)

The test specimens were removed from the storage tank immediately prior to the test. Initial values

of length and diameter were obtained and the specimen was placed in the test cell. Porous metal discs approximately 0.10 inch thick and with a diameter equal to the specimen diameter were placed at either end of the specimen to provide drainage for any pore fluids expelled during the test. The upper load platen, load cell, and axial deformation transducer were mounted and the cell centered in the loading bed of the 300 kip loading machine. The three channels of information from the test were connected to the plotter such that the load was plotted along the X axis, the axial deformation along the Y axis, and the lateral deformation along the Y' axis.

All specimens were subjected to an initial load-unload cycle of 500 lbs. to seat the specimen. The hydrostatic loading was obtained by increasing or decreasing the axial load and the fluid confining pressure in unison. By using a relatively slow rate of loading, the two resulting stresses could be maintained equal to within 100 psi. The hydrostatic stress was applied at an approximate rate of 500 psi per minute. All hydrostatic loadings were conducted with the three channels of the plotter set at the most sensitive setting of 1 mv/inch.

Hydrostatic stresses were increased to levels of 2500 psi, 5000 psi, and 7500 psi, at which point the lateral confining pressure was maintained at a constant level. The axial load was increased until failure, characterized by a drop in axial load resistance, or a yielding behavior, characterized by constant load resistance under increasing axial deformation, was observed. Except for specimen No. 5, the plotter sensitivity for all channels was set to a

reduced sensitivity of 10 mv/inch for the deviatoric loading. The deviatoric loading was conducted at a rate such that the axial strain rate was on the order of 10^{-4} per second.

The uniaxial tests contained in the program on the Series I and Series II rocks were conducted following the same procedures as used for the triaxial tests except that they were conducted with all data channels set at the 1 mv/inch scale.

Data Reduction

A. Hydrostatic Loading

Data from the hydrostatic loading phase of a test was reduced to yield a value of volumetric strain, $\Delta V/V_o$, at each 250 psi increment of hydrostatic loading. The axial strain was computed using the recorded chart response, the calibration factor of the axial cantilevers, and specimen length. A correction for the apparent strain resulting from axial compression of the steel platens and porous steel discs was included in the calculation. The radial specimen strain was computed using the recorded chart response, the lateral cantilever calibration factor, the measured cell deformation calibration, and the pressure and the specimen diameter. From the calculated values of axial and radial strain, both the volume change, ΔV, and the volumetric strain, $\Delta V/V_o$, were computed. A programmable hand calculator was used for the data reduction.

B. Deviatoric Loading

The recorded chart data from the deviatoric loading phase was reduced to yield values of deviatoric axial and lateral strain vs. deviatoric stress. The correction factor for compression of the steel platens was again included in the data reduction procedure for axial strain. As the lateral confining pressure was maintained constant during the deviatoric loading, the correction factor for cell expansion was not necessary.

Results - Triaxial Tests

The dimensions of the specimens and total failure stress computed using both the peak value of stress and the value at 0.002 strain offset are given in Table I. The 0.002 strain offset was taken to be parallel to the axial stress - axial strain curve where no initial stiffening behavior was observed. Where the initial stiffening behavior was noted, the offset was taken parallel to the initial linear portion of the stress-strain curve. For three of the tests with $\sigma_3 = 0$, specimen failure occurred before the 0.002 offset strain point. In Table II are presented the values of the bulk modulus, K, determined from the linear range of response and the elastic parameters, E, Young's modulus, and ν, Poisson's ratio, determined from tangent values at 50% of the peak deviatoric stress.

Plots of the hydrostatic loading response in the form of $\Delta V/ V_o$ versus hydrostatic stress are presented in Figures 2 to 15. Plots of axial strain

and lateral strain versus deviatoric stress are contained in Figures 16 to 31. The raw data plots from the X-Y-Y' recorder are contained in the Appendix.

Discussion of Results

The bulk modulus, K, determined from the hydrostatic loading phase of the tests ranged from 231 ksi to 588 ksi with an average value of 361 ksi for the 14 determinations available. These values were determined for that portion of the curve which had the most linear response. The effects of initial low modulus values, the abrupt stiffening noted in Specimen 10, 13, and 15, and the softening noted at high stress levels in Specimens 1 and 17 were thus excluded in the determination of the bulk modulus.

The values of Young's modulus, E, and Poisson's ratio, ν, determined from tangent values at a stress level equal to 50% of the peak deviatoric stress value, show considerable scatter ranging from 152 ksi to 565 ksi for E and from 0.19 to 0.73 for ν. In Figure 32, values of Young's modulus are plotted versus confining pressure. A trend of decreasing modulus with increasing values of confining pressure is seen. The Series II rock shows a stronger relationship than the Series I rock. A similar plot of Poisson's ratio versus confining pressure is presented in Figure 33. The Series I rock shows a significant increase in Poisson's ratio with increasing confining pressure whereas the Series II material exhibits no relationship between Poisson's ratio and confining pressure.

The peak failure stresses from the deviatoric loadings are plotted versus confining pressure in Figure 34. A visual fit of a straight line to this data provides the following strength relation: $\sigma_f = 2{,}000 + 1.5$ (psi). Material from the two rock batches tested show no decernable difference with respect to peak strength.

Directional Property Study

To investigate possible anisotropy of the tuff rock, a series of uniaxial and tensile splitting tests were run on Series II rock. An orthogonal X-Y-Z coordinate system was established with the Z axis along the 6" diameter core axis and with the X and Y axes arbitrarily orientated. Because the individual pieces of the 6 inch core were not match marked, the X and Y axes chosen for the uniaxial specimens may not correspond to those selected for the tensile tests as two different pieces of 6" core were used to prepare specimens.

Results from the uniaxial tests are presented in Table III. Specimen No. 19, originally planned for a triaxial test, was inadvertenly subjected to a uniaxial test and is therefore included in those results. The data indicate that both the uniaxial strength and Young's Modulus show a directional variation with the Z axis having the greatest strength and modulus. Since the X-Y axes were arbitraily chosen, it is possible that a greater degree of anisotropy could have been measured with a different X-Y axes orientation.

Although the above data indicates directional properties exist, the number of tests are inadequate to accurately define the directional values of the uniaxial strength and modulus.

Specimens for the Brazilian tensile splitting test were prepared from NX size core drilled parallel (Z axis) and perpendicular (X and Y axes) to the axis of the 6" core. For each Brazilian disk, two

possible orientations of the tensile failure plane are possible. For example, a disk from a X core could be tested to measure tensile strength along either the X-Z plane or the X-Y plane.

The orientation of the X-Y-Z coordinate system was maintained on all disc specimens. Using all of the remaining 6 inch core, it was possible to prepare a total of 24 tensile specimens which were equally divided between the X, Y, and Z orientations. Equal numbers of specimens from each coring direction were tested in each of the two possible directions as described above.

Tensile test specimens were stored under water until shortly before testing. Specimen thickness was measured and the disk was wrapped with a double thickness of masking tape. All specimens were from NX core having a diameter of 2.137 inch. Specimens were tested in a tensile test loading device meeting the requirements of the ISRM "Suggested Methods for Determination of Tensile Strength". Data was reduced using the formula $\sigma_t = 0.636\ P/Dt$ where P is the failure load, D the specimen diameter and t is the specimen thickness.

Results of the individual tests are presented in Table III. From the individual test results the following average values of tensile strength are obtained:

Direction of Tensile Stress	Failure Plane	Tensile Strength, psi
X	Y-Z	223
Y	X-Z	226
Z	X-Y	238

No directional variation in tensile strength is apparent in the above data.

TABLE I

SPECIMEN DIMENSION AND STRENGTH DATA

Specimen No.	Series No.	Diameter -inches	Length -inches	Confining Pressure -psi	Failure Stress Peak-psi	Failure Stress .002 offset psi
1	I	2.132	3.55	hydrostatic test only		
2	I	2.130	3.13	hydrostatic test only		
3	I	2.133	3.059	0	2130	2130
4	I	2.133	4.148	0	2270	-
5	I	2.137	4.084	2500	7060	6290
6	I	2.137	4.187	2500	6050	5540
7	I	2.135	4.121	5000	9570	9130
8	I	2.132	4.340	5000	8690	7950
9	I	2.137	4.186	7500	13,320	12,000
10	I	2.137	4.082	7500	12,560	12,220

TABLE I (cont.)

SPECIMEN DIMENSION AND STRENGTH DATA

Specimen No.	Series No.	Diameter -inches	Length -inches	Confining Pressure -psi	Failure Stress Peak-psi	Failure Stress .002 offset psi
11	II	2.138	4.246	0	2000	-
12	II	2.138	4.250	0	1490	-
13	II	2.138	4.222	2500	7260	6970
14	II	2.138	4.175	2500	6090	5130
15	II	2.141	4.324	5000	9230	7720
16	II	2.135	4.200	5000	8680	7680
17	II	2.138	4.303	7500	12,810	10,150
19	II	2.138	4.219	0	2400	-
20	II	2.139	4.167	7500	12,710	10,150
Ia	II	2.136	4.422	0	1640	-
Ib	II	2.136	4.300	0	1710	-
IIa	II	2.135	4.257	0	1340	-
IIb	II	2.135	4.265	0	1390	-

Atkinson-Noland & Associates, Inc./Consulting Engineers

TABLE II
STIFFNESS DATA

Specimen No.	Series No.	Hydrostatic Bulk Modulus-ksi	Deviatoric Young's Modulus-ksi	Deviatoric Poisson's Ratio
1	I	288	-	-
2	I	231	-	-
3	I	-	405	.19
4	I	-	596	.31
5	I	294	519	.37
6	I	405	316	.32
7	I	465	477	.57
8	I	349	377	.61
9	I	352	364	.73
10	I	517	565	.57
11	II	-	460	.24
12	II	-	333	.33
13	II	588	538	n.a.
14	II	300	436	.22
15	II	328	342	.35
16	II	325	317	.32
17	II	288	152	.31
20	II	323	152	.28

TABLE III
UNIAXIAL DIRECTIONAL PROPERTIES
SERIES II ROCK

Core Axis	Specimen No.	σ_f psi	Modulus, E psi
X	Ia	1640	391,750.
	Ib	1710	396,200.
Y	IIa	1340	279,100.
	IIb	1390	302,400.
Z	11	2000	459,850.
	12	1490	330,800.
	19	2400	478,550.

TABLE IV

BRAZILIAN TENSILE TEST DATA

Spec. No.	Axis	Failure Plane	σ_t Dir.	t inch	P lbs.	σ_t psi
1	X	X-Z	Y	1.016	700	205
2	X	X-Z	Y	.933	780	248
3	X	X-Z	Y	.986	620	187
4	X	X-Z	Y	1.011	820	241
5	X	X-Y	Z	1.027	990	287
6	X	X-Y	Z	.855	660	230
7	X	X-Y	Z	1.014	740	217
8	X	X-Y	Z	1.038	1320	378
9	Y	Y-Z	X	1.067	720	201
10	Y	Y-Z	X	1.075	820	227
11	Y	Y-Z	X	.996	620	185
12	Y	Y-Z	X	.981	900	273
13	Y	Y-X	Z	1.044	840	239
14	Y	Y-X	Z	1.012	660	194
15	Y	Y-X	Z	.972	620	190
16	Y	Y-X	Z	1.047	580	165
17	Z	Z-X	Y	1.065	800	223
18	Z	Z-X	Y	1.020	760	222
19	Z	Z-X	Y	1.043	820	234
20	Z	Z-X	Y	.972	820	251

TABLE IV (cont.)
BRAZILIAN TENSILE TEST DATA

Spec. No.	Axis	Failure Plane	σ_t Dir.	t inch	P lbs.	σ_t psi
21	Z	Z-Y	X	1.001	820	244
22	Z	Z-Y	X	1.007	780	230
23	Z	Z-Y	X	.997	640	191
24	Z	Z-Y	X	1.077	840	232

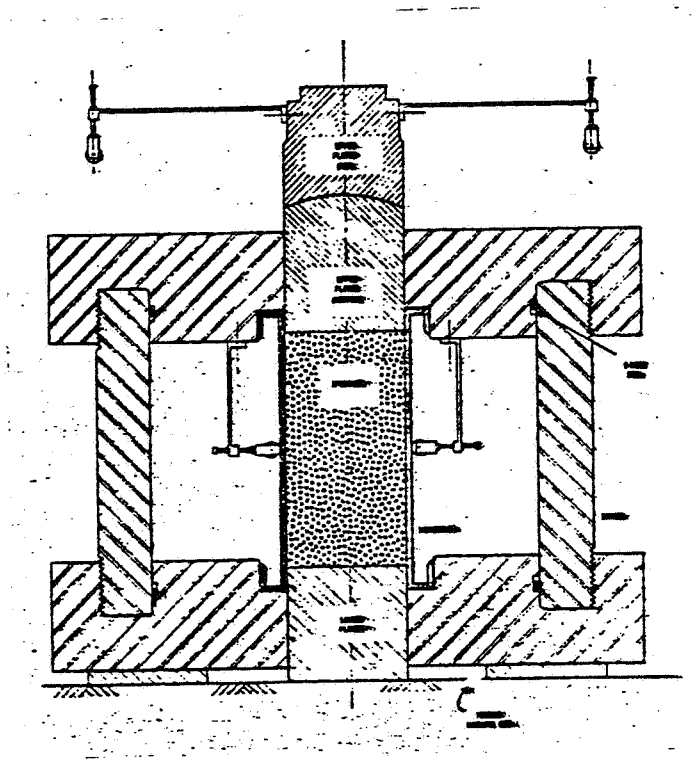

SECTION VIEW OF TRIAXIAL CELL

FIGURE 1

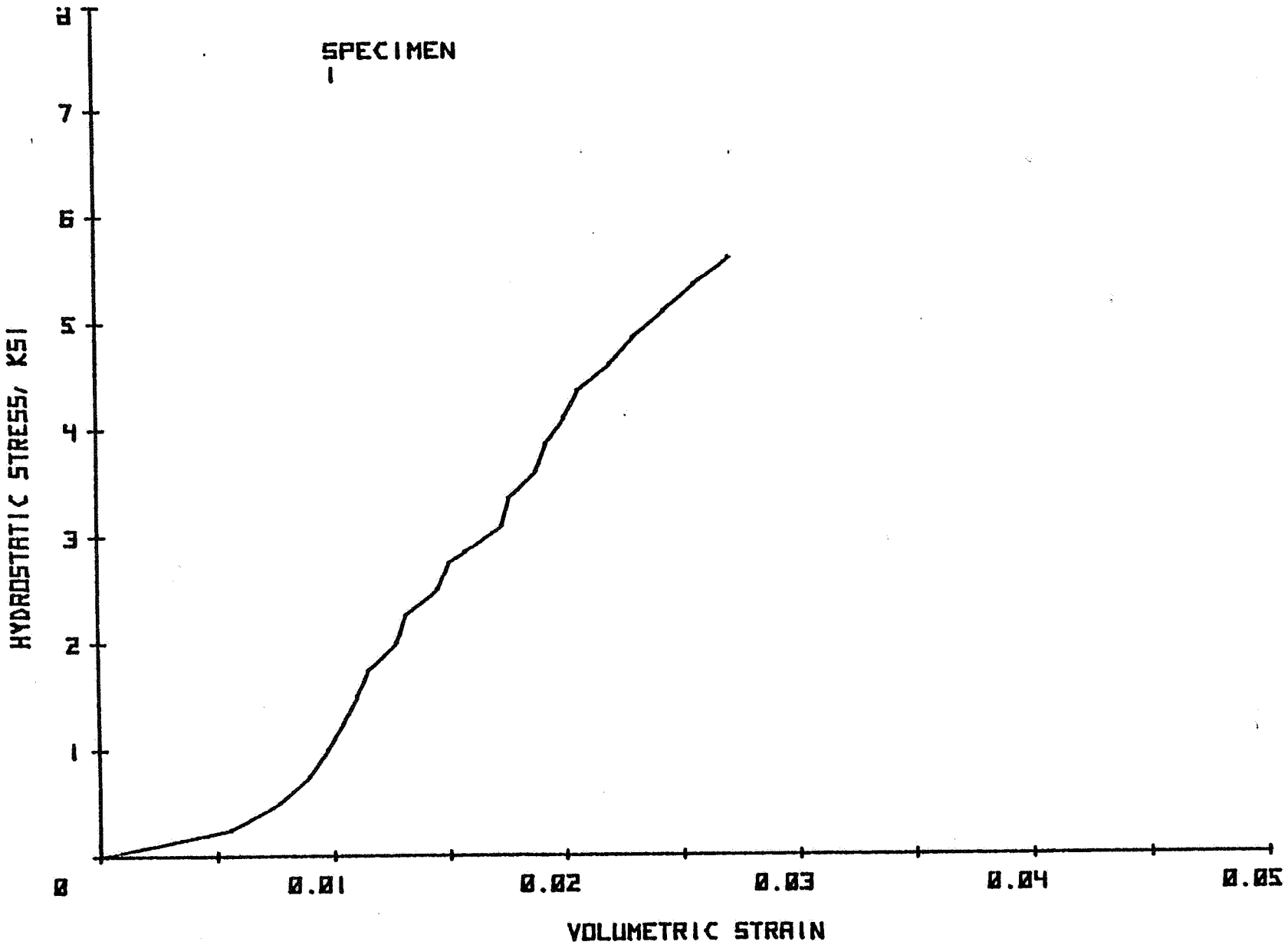

Hydrostatic Responce, Specimen 1
Figure 2

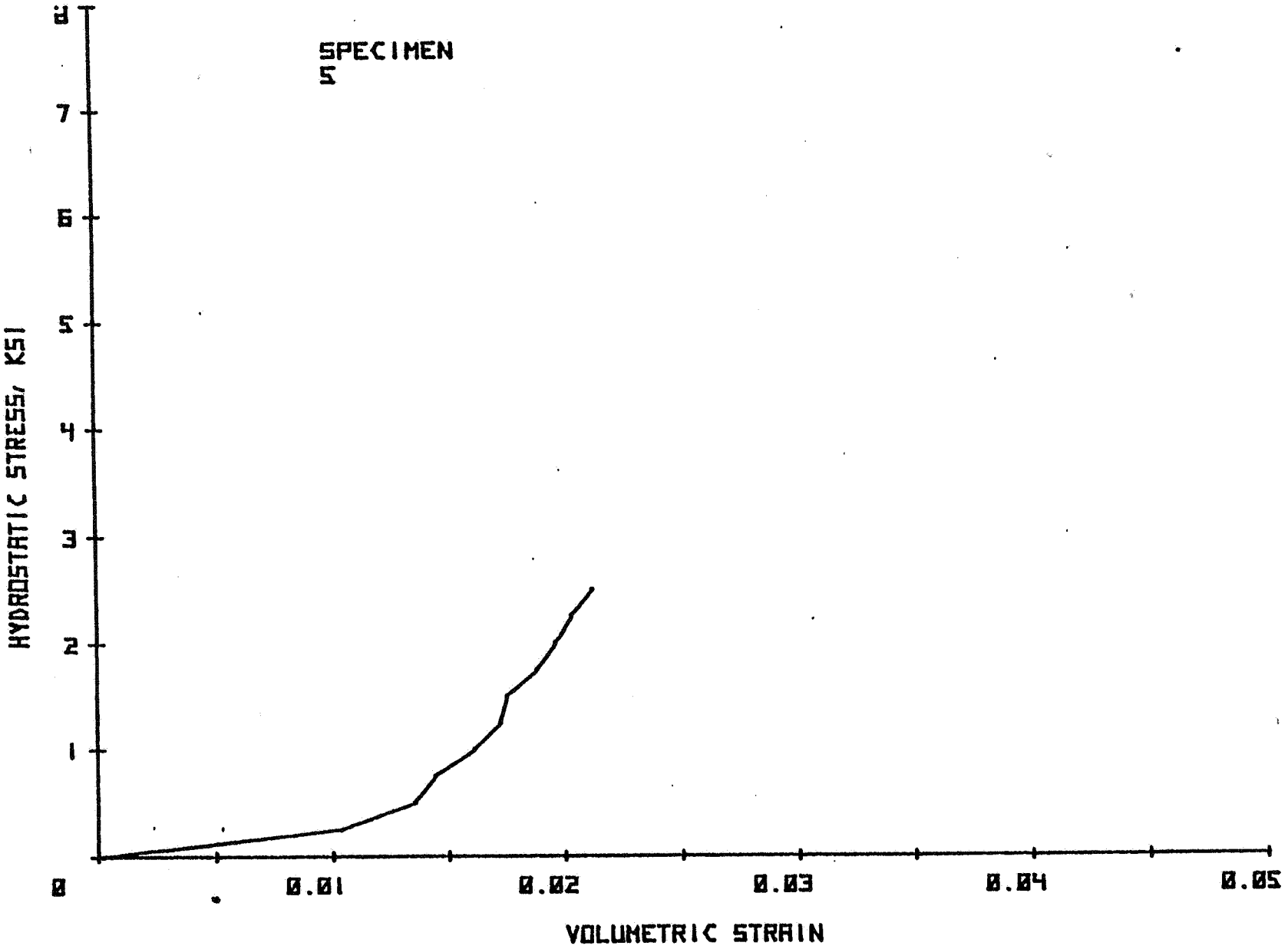

Hydrostatic Response, Specimen 5
Figure 4

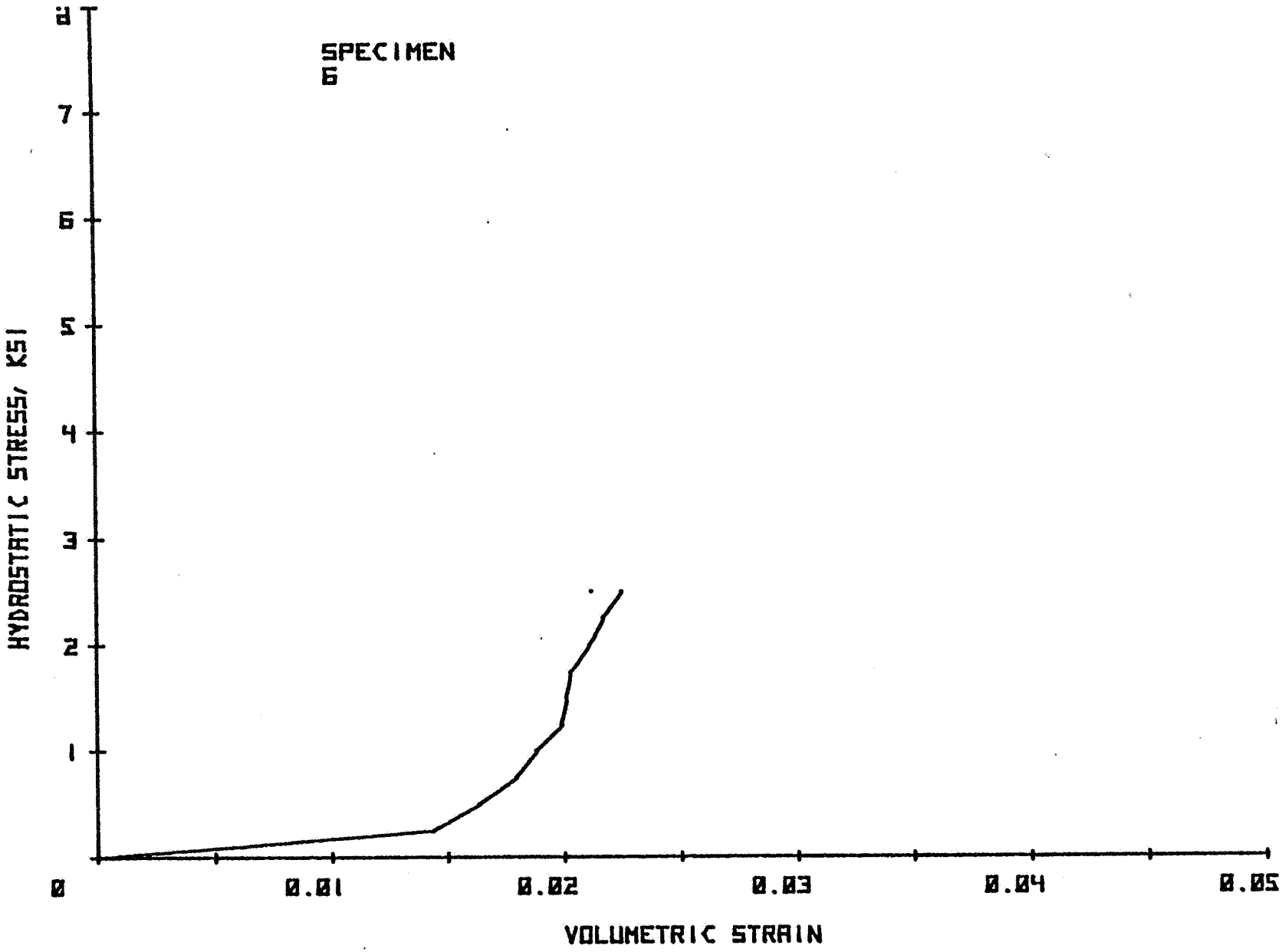

Hydrostatic Response, Specimen 6
Figure 5

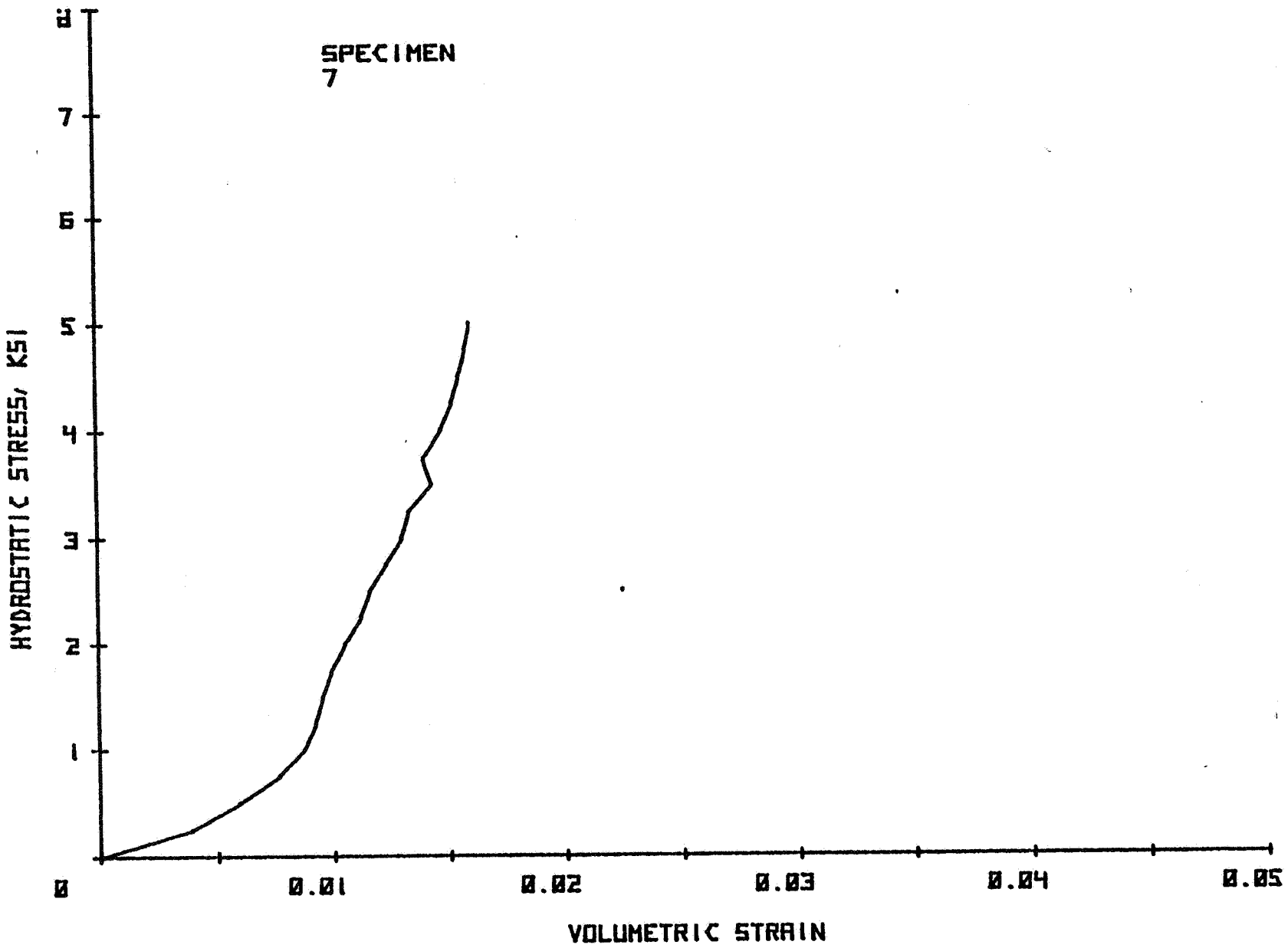

Hydrostatic Response, Specimen 7
Figure 6

Atkinson-Noland & Associates, Inc./Consulting Engineers

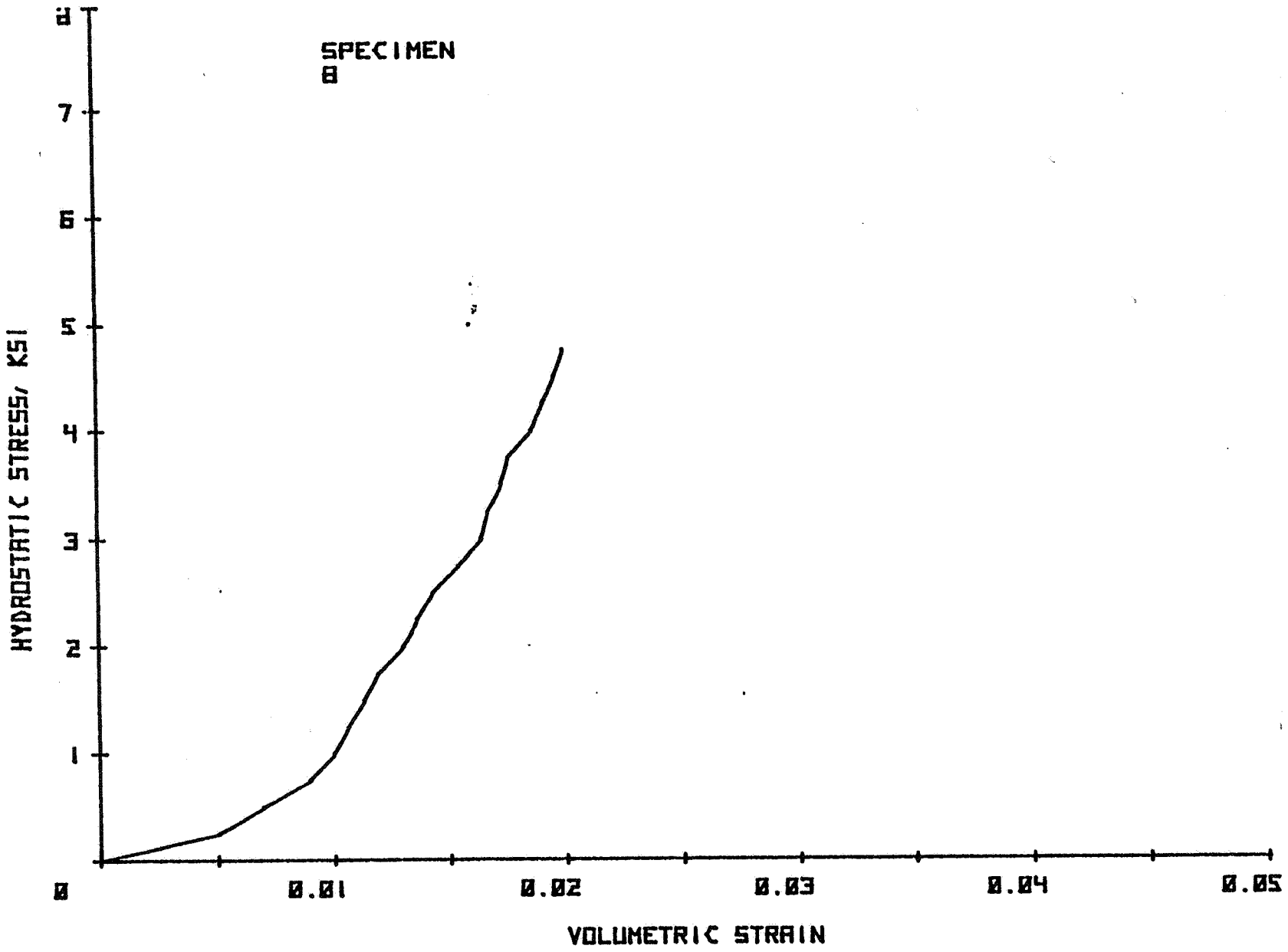

Hydrostatic Response, Specimen 8
Figure 7

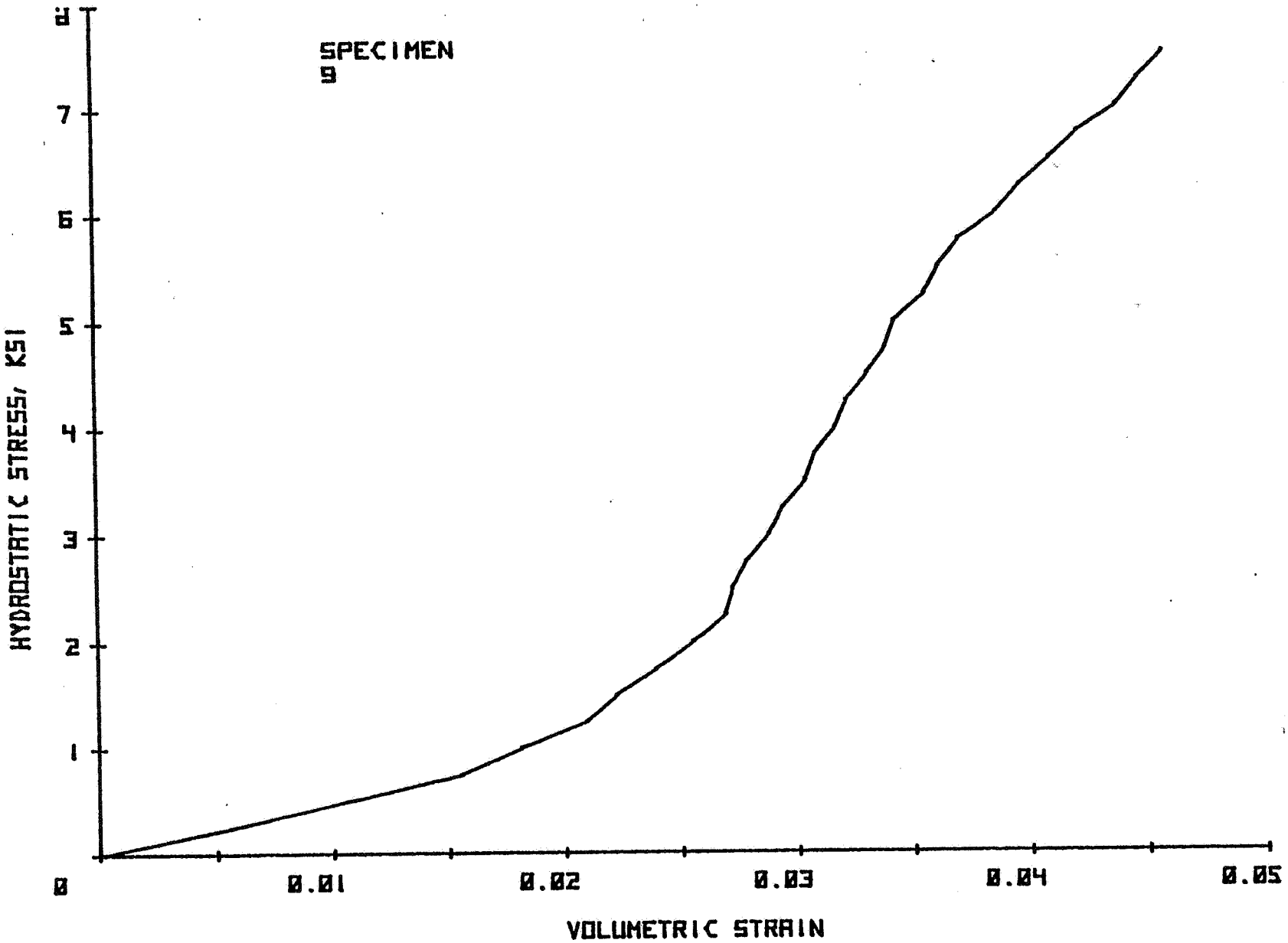

Hydrostatic Response, Specimen 9
Figure 8

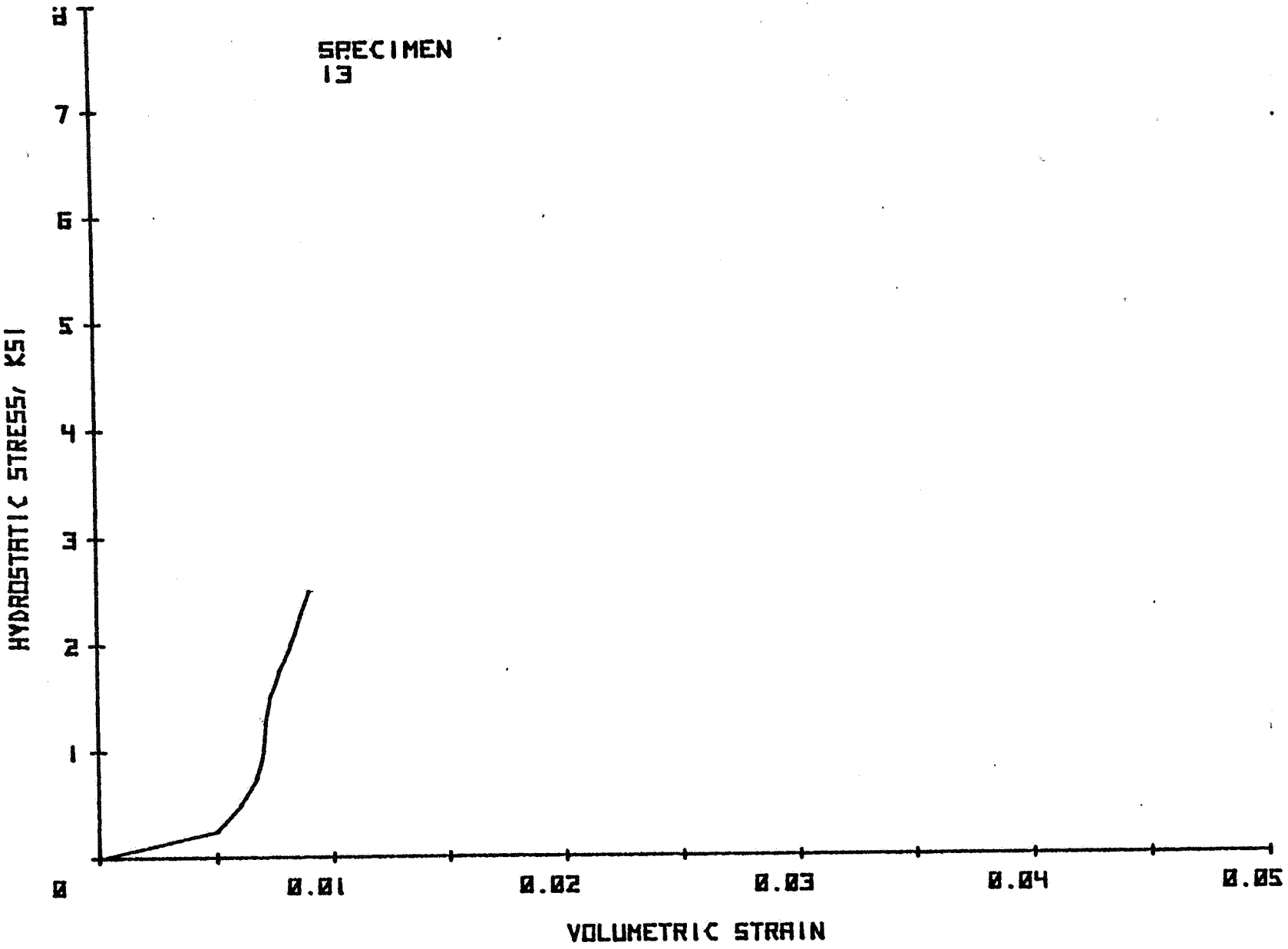

Hydrostatic Response, Specimen 13
Figure 10

Atkinson-Noland & Associates, Inc./Consulting Engineers

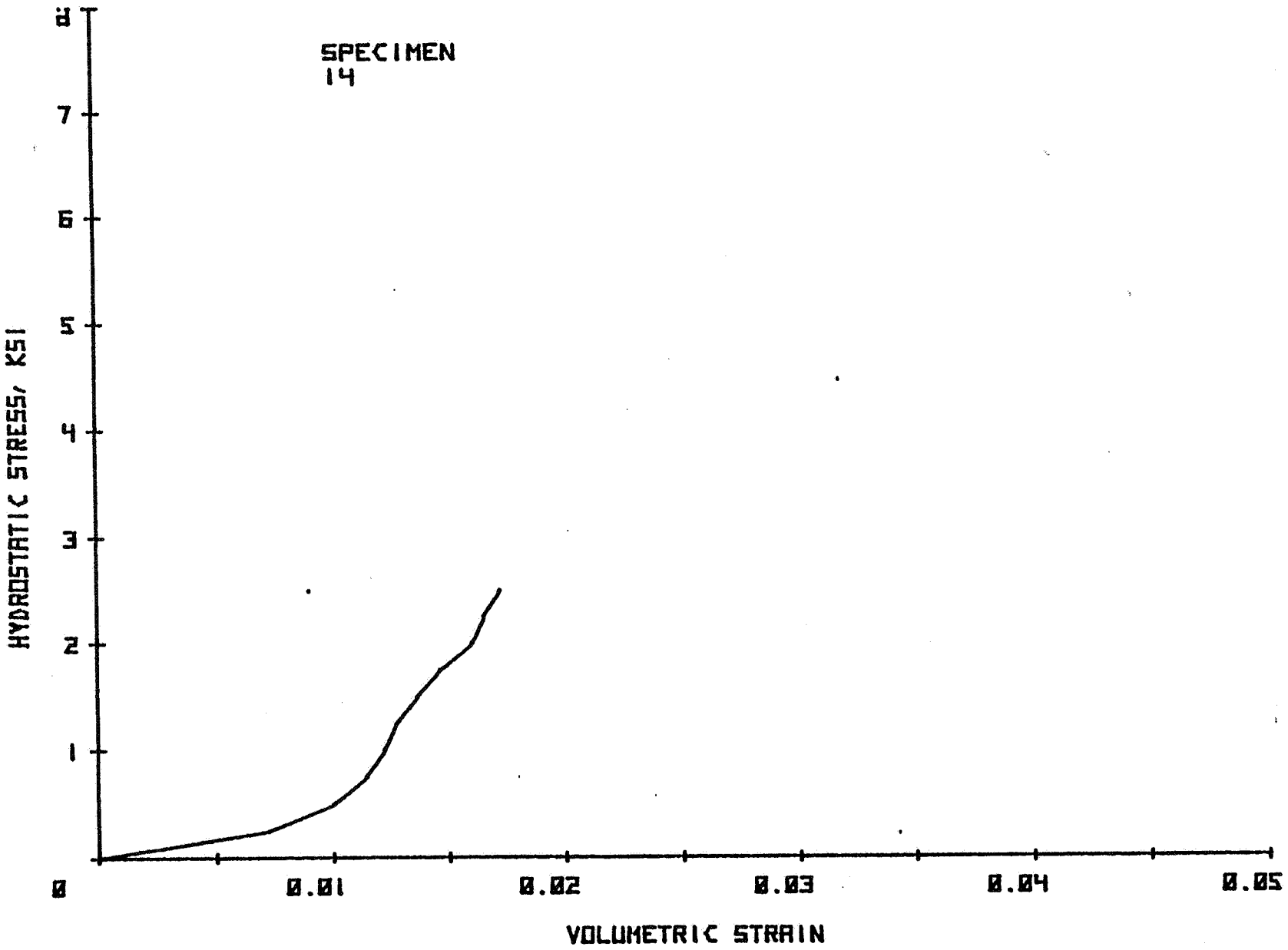

Hydrostatic Response, Specimen 14

Figure 11

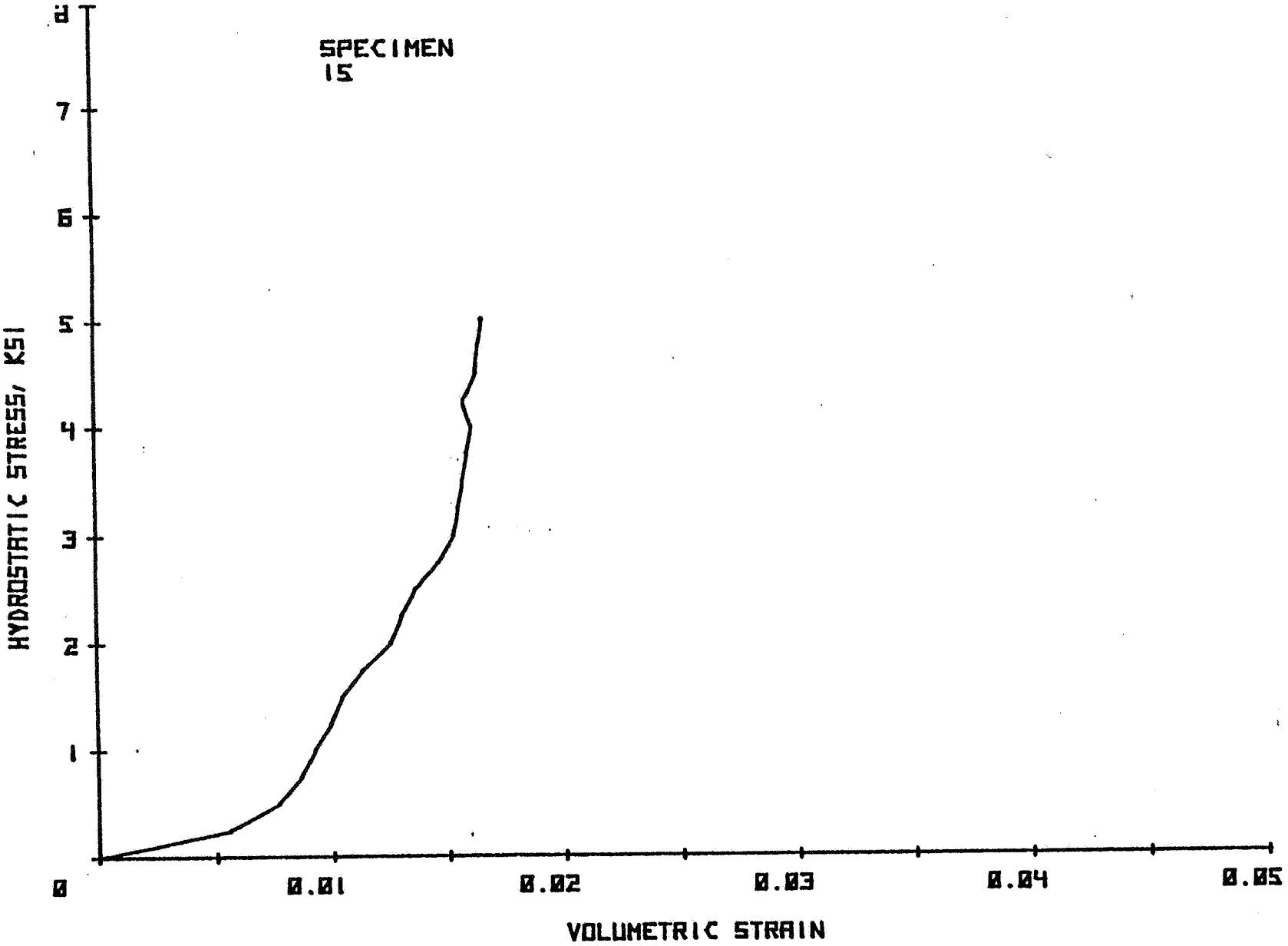

Hydrostatic Response, Specimen 15
Figure 12

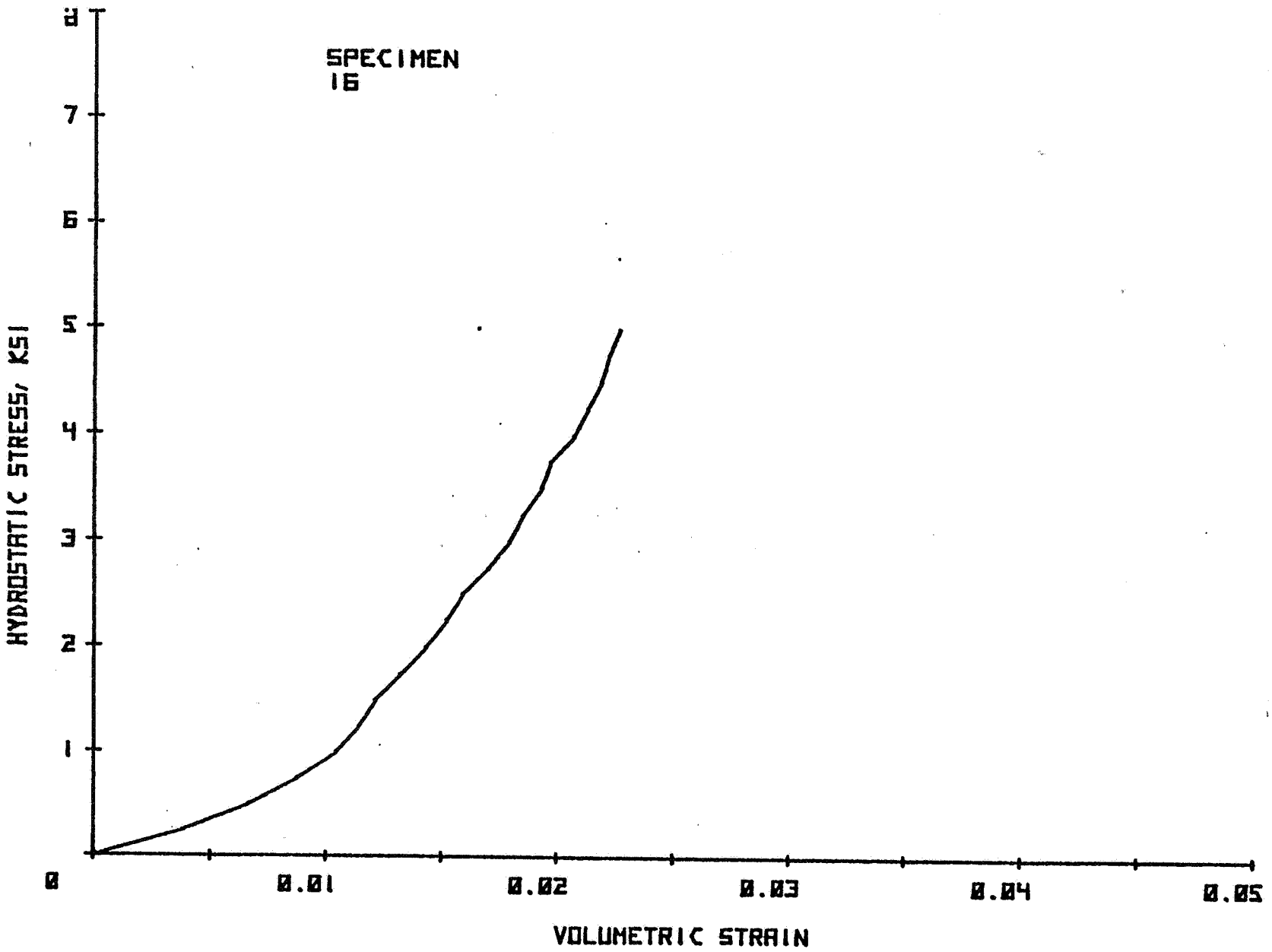

Hydrostatic Response, Specimen 16
Figure 13

Atkinson-Noland & Associates, Inc./Consulting Engineers.

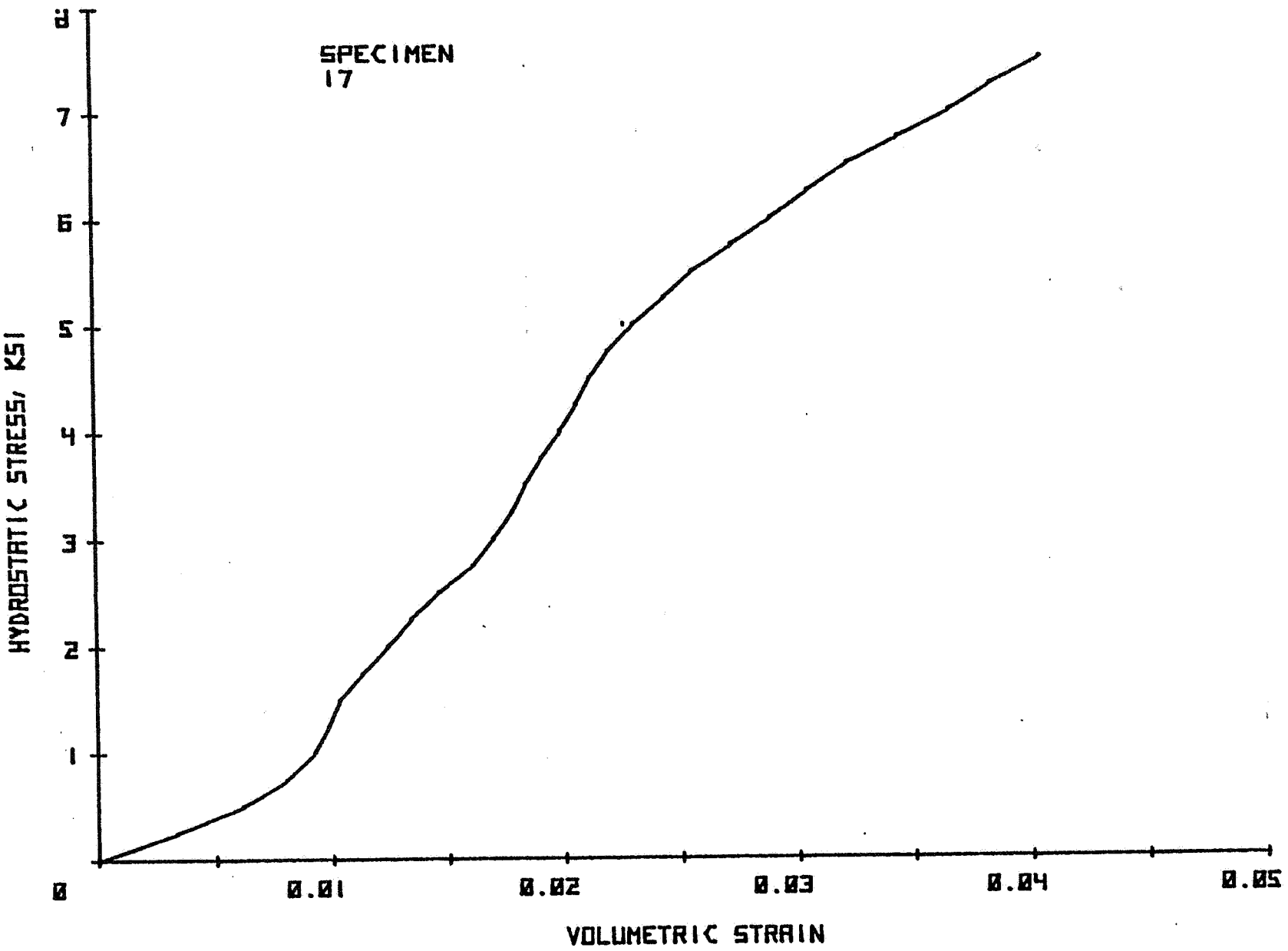

Hydrostatic Response, Specimen 17

Figure 14

Atkinson-Noland & Associates, Inc./Consulting Engineers

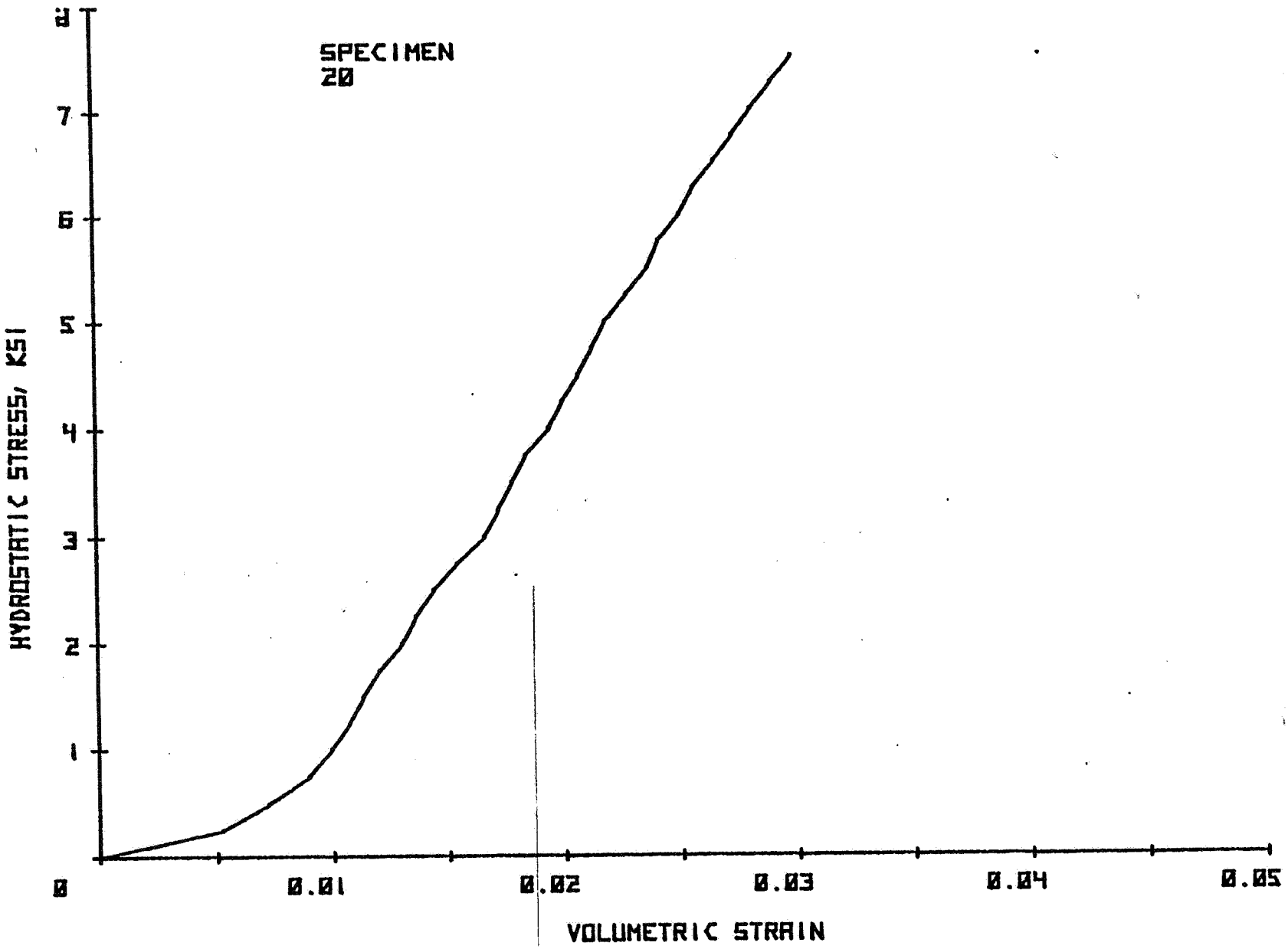

Hydrostatic Response, Specimen 20
Figure 15

Atkinson-Noland & Associates, Inc./Consulting Engineers

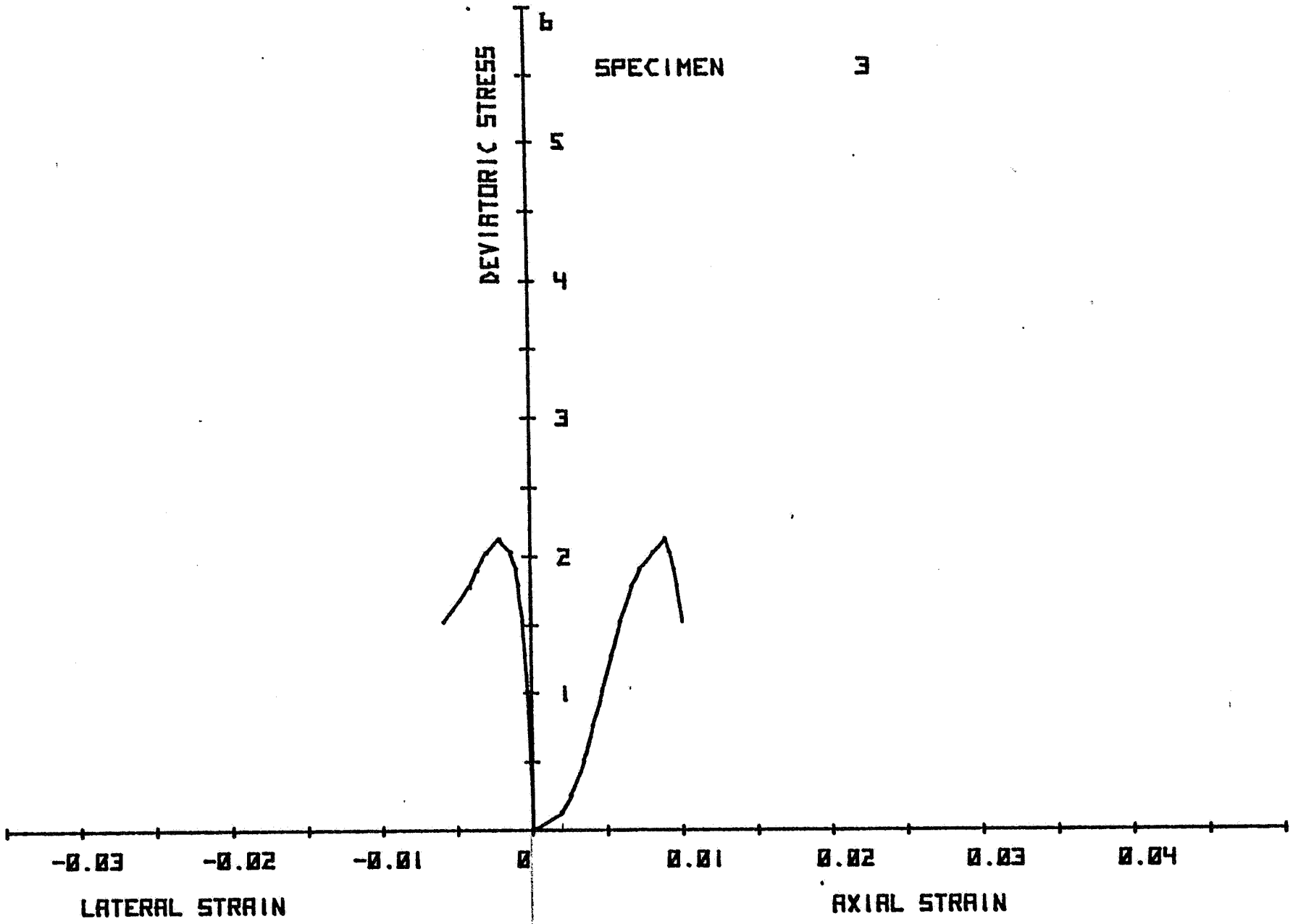

Deviatoric Response, Specimen 3
Figure 16

Atkinson-Noland & Associates, Inc./Consulting Engineers

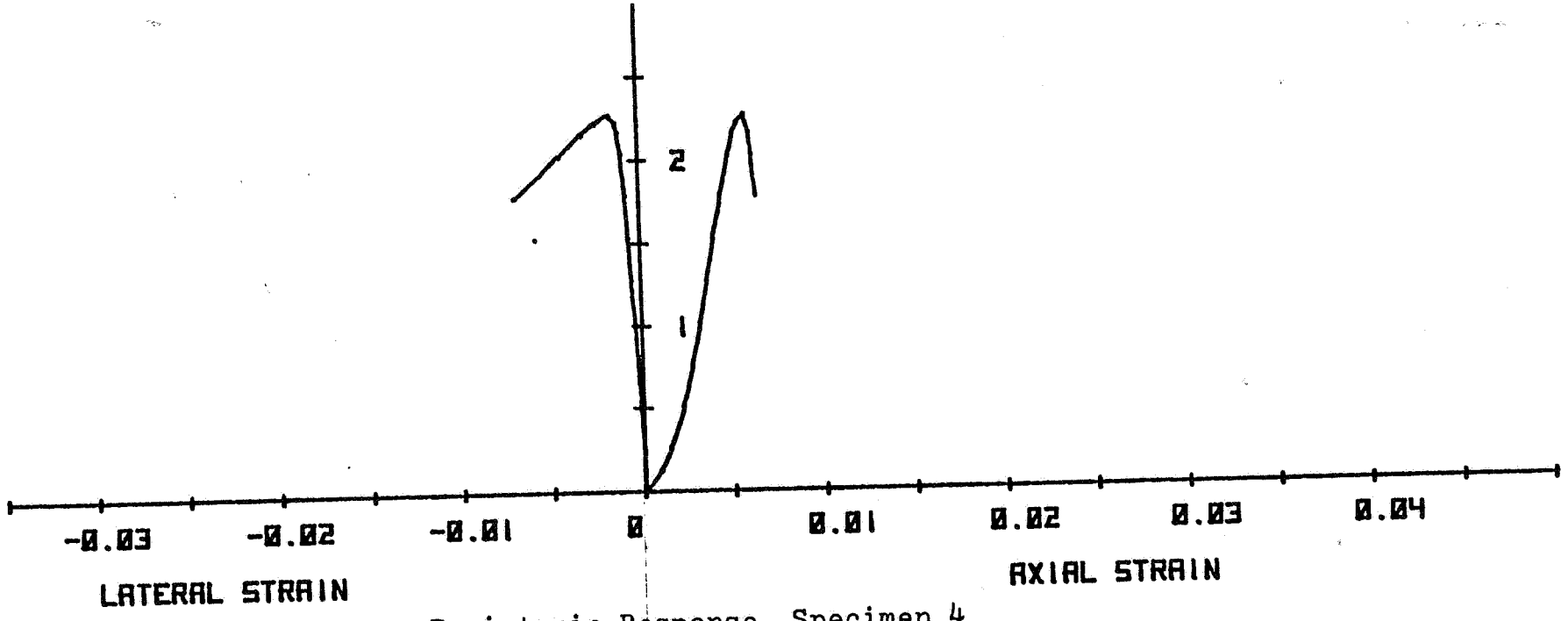

Deviatoric Response, Specimen 4
Figure 17

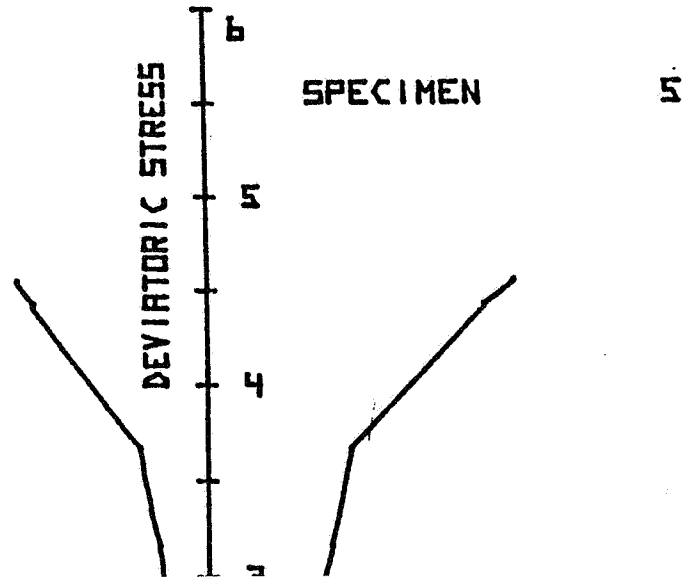

s Inc. /Consulting Engineers Atkinson-Noland & Associate

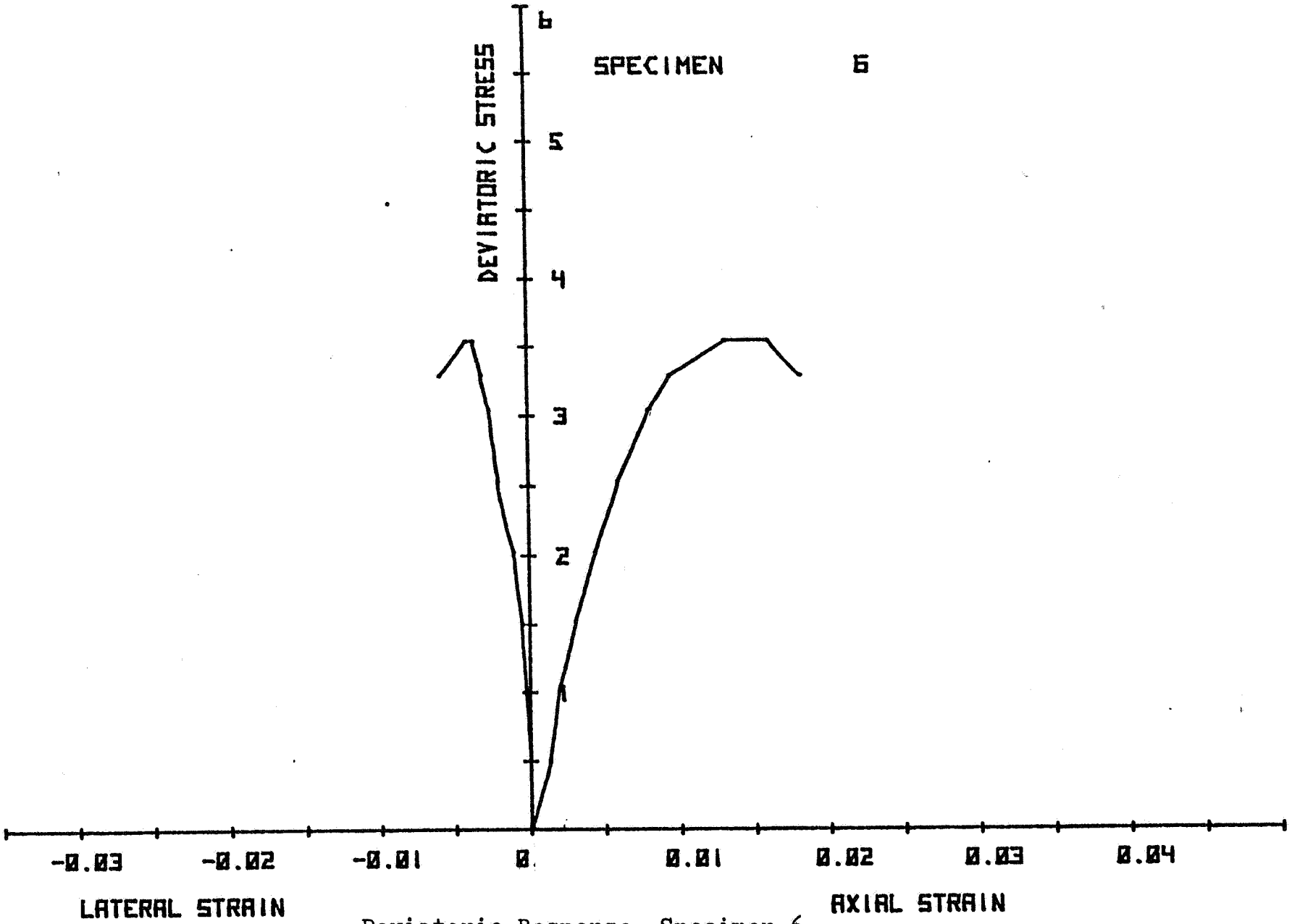

Deviatoric Response, Specimen 6
Figure 19

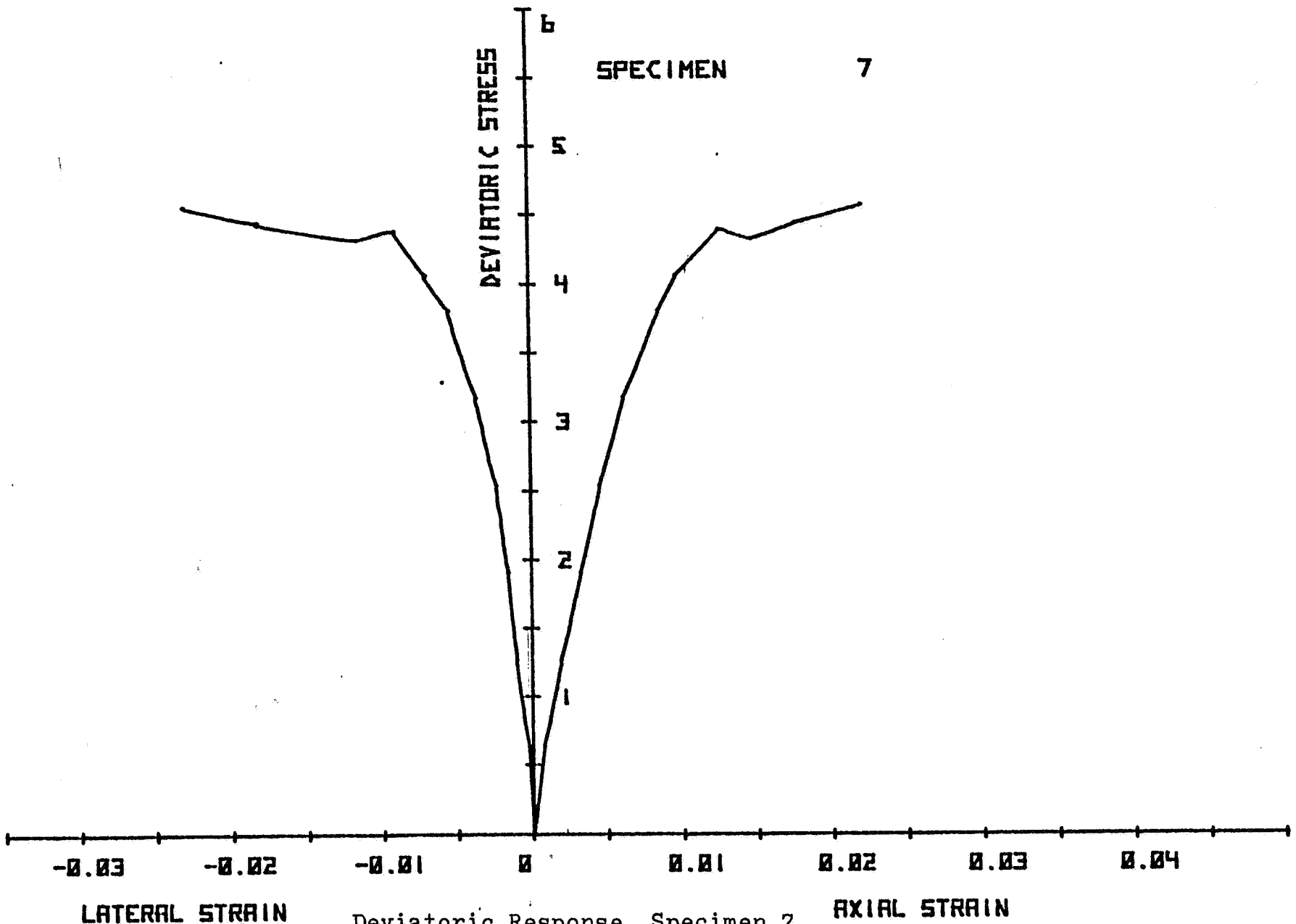

Deviatoric Response, Specimen 7
Figure 20

Atkinson-Noland & Associates, Inc./Consulting Engineers

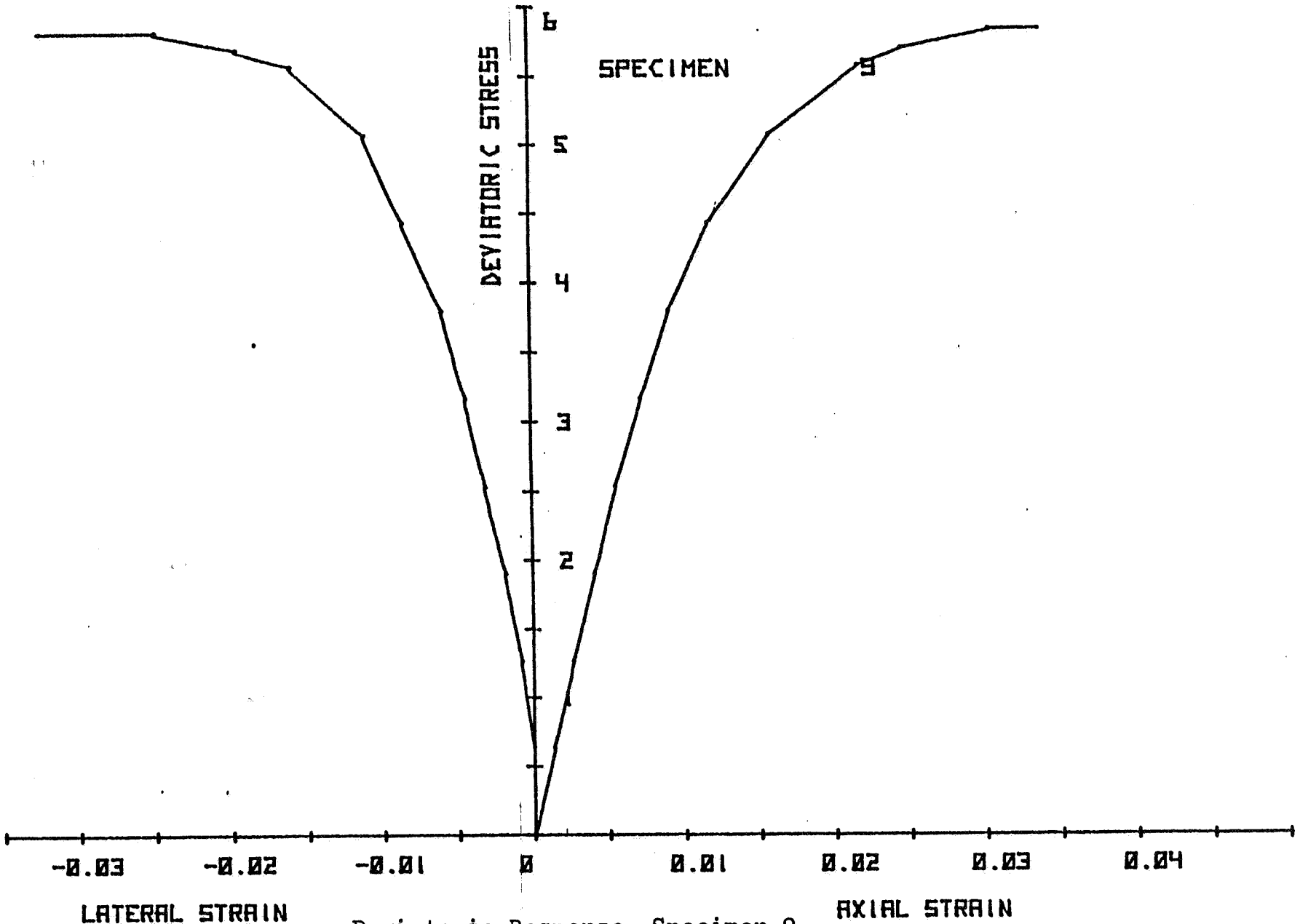

Deviatoric Response, Specimen 9
Figure 22

Atkinson-Noland & Associates, Inc./Consulting Engineers

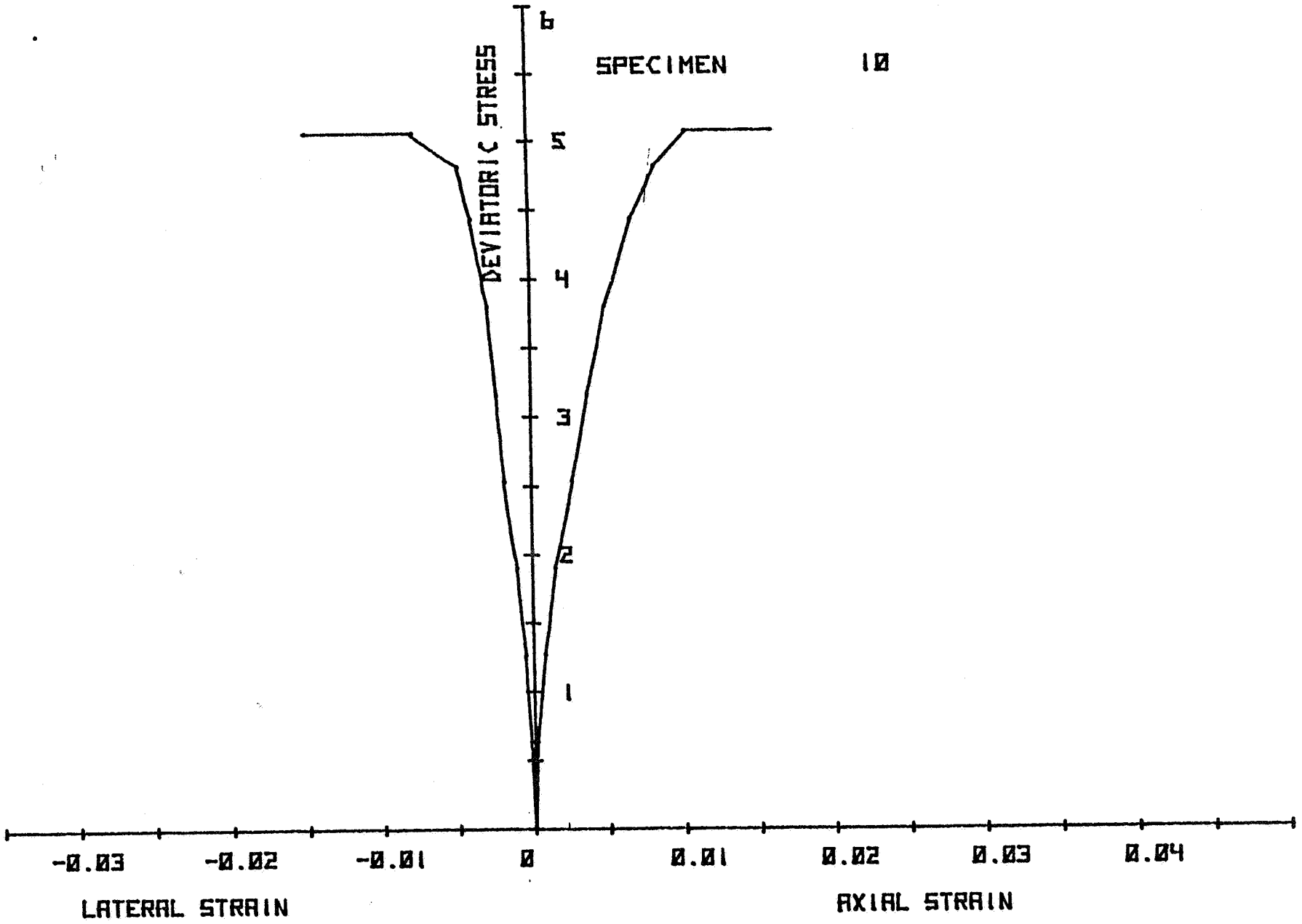

Deviatoric Response, Specimen 10
Figure 23

Atkinson-Noland & Associates, Inc./Consulting Engineers

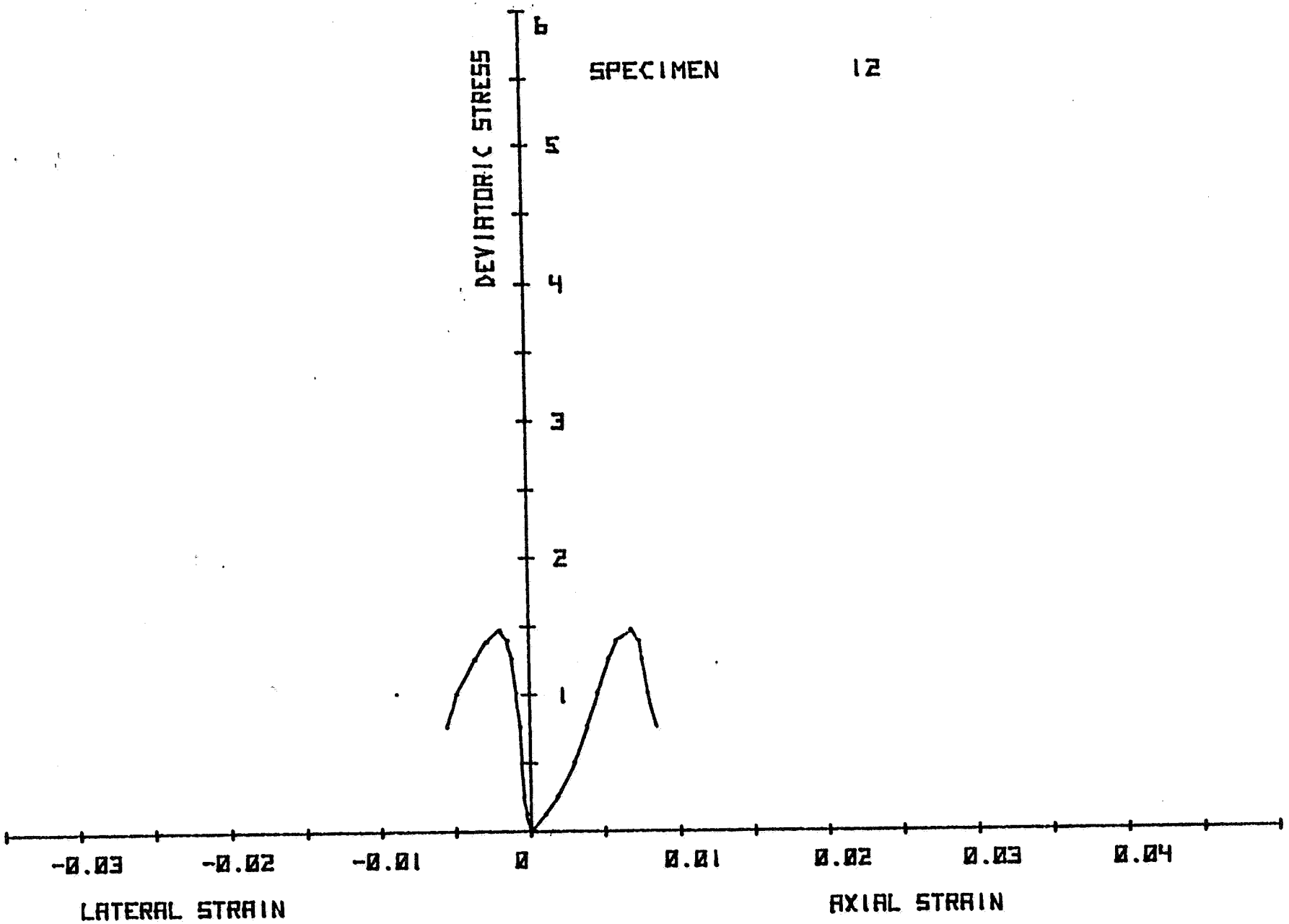

Deviatoric Response, Specimen 12
Figure 25

Atkinson-Noland & Associates, Inc./Consulting Engineers

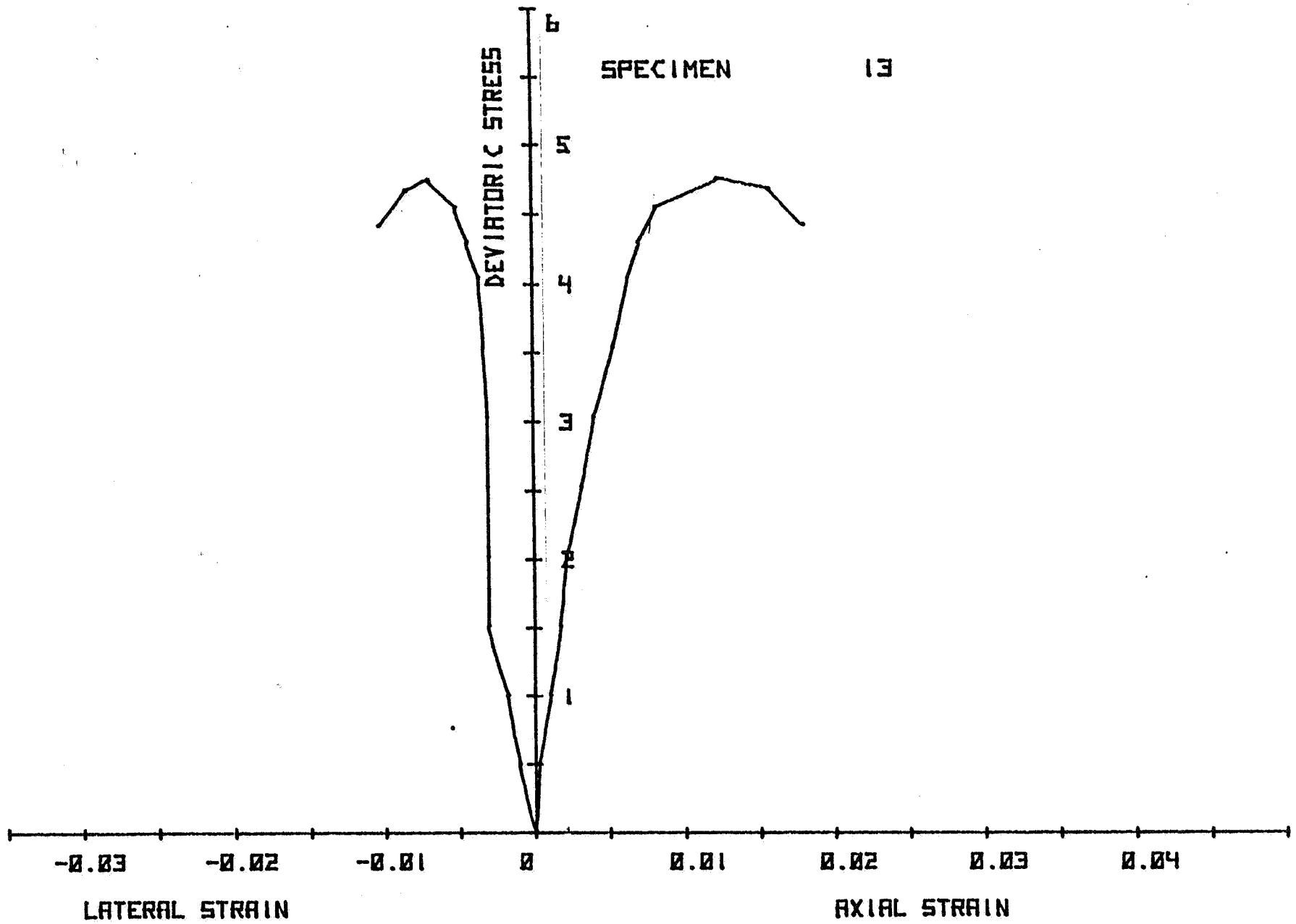

Deviatoric Response, Specimen 13
Figure 26

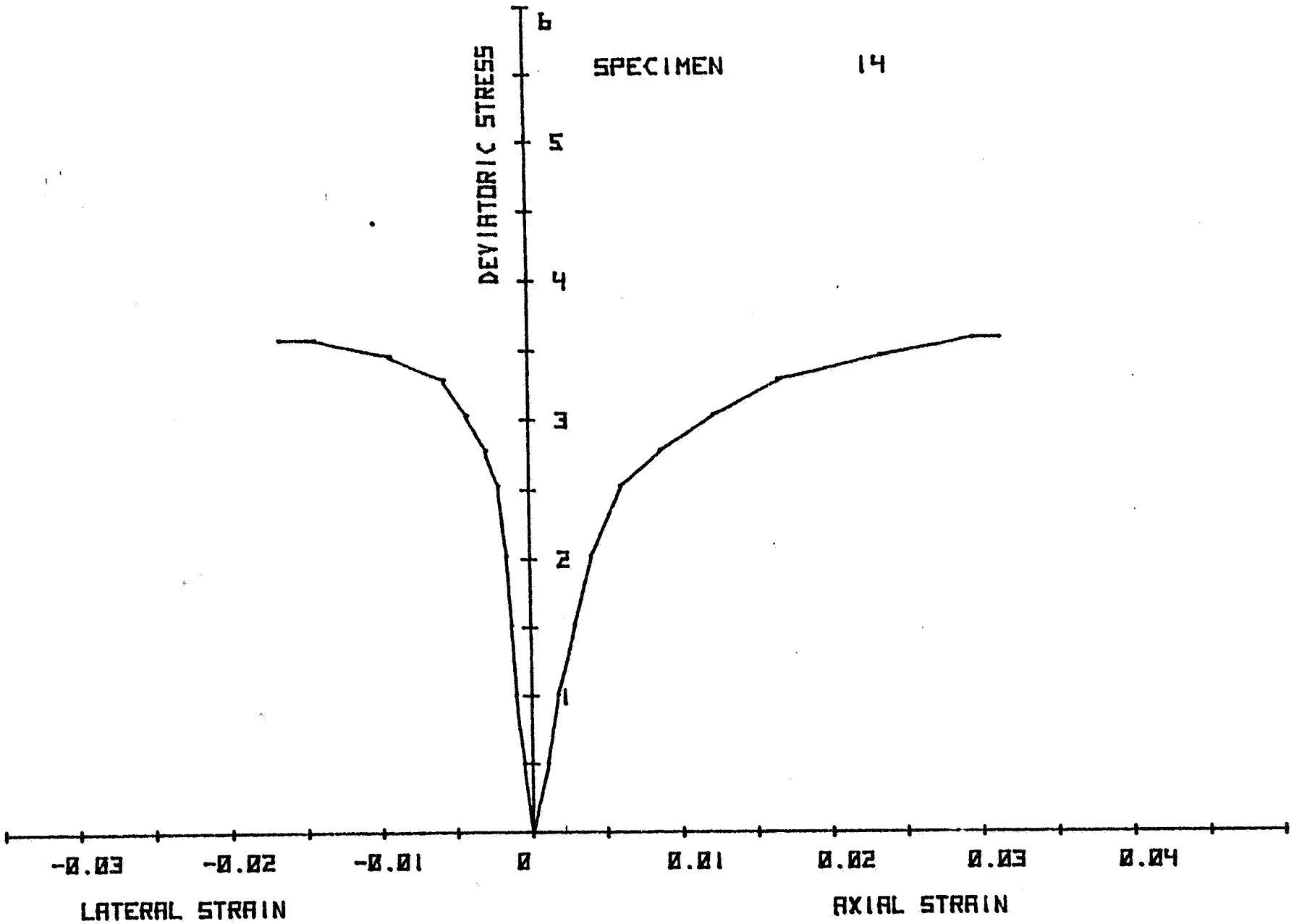

Deviatoric Response, Specimen 14
Figure 27

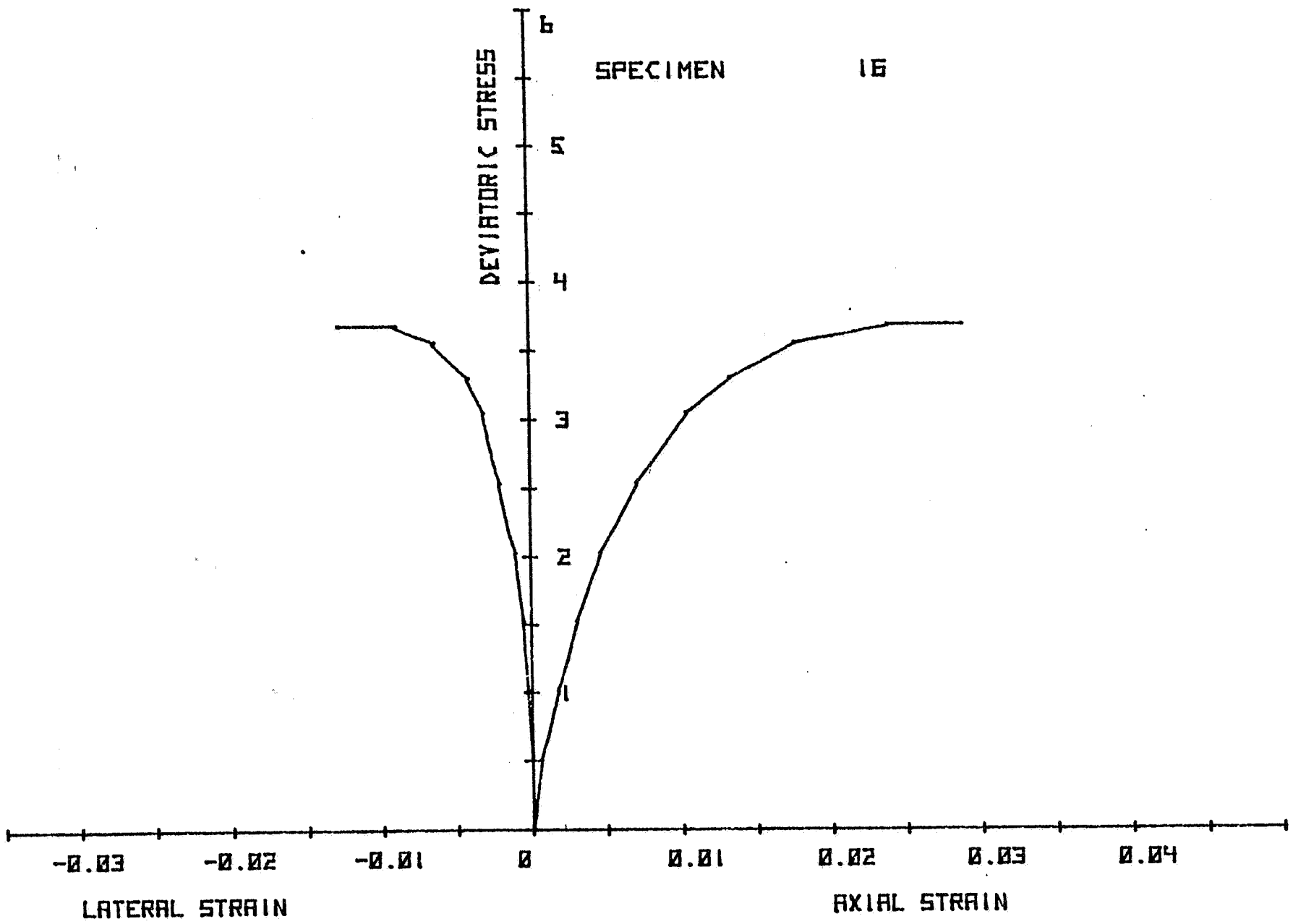

Deviatoric Response, Specimen 16
Figure 29

Atkinson-Noland & Associates, Inc./Consulting Engineers

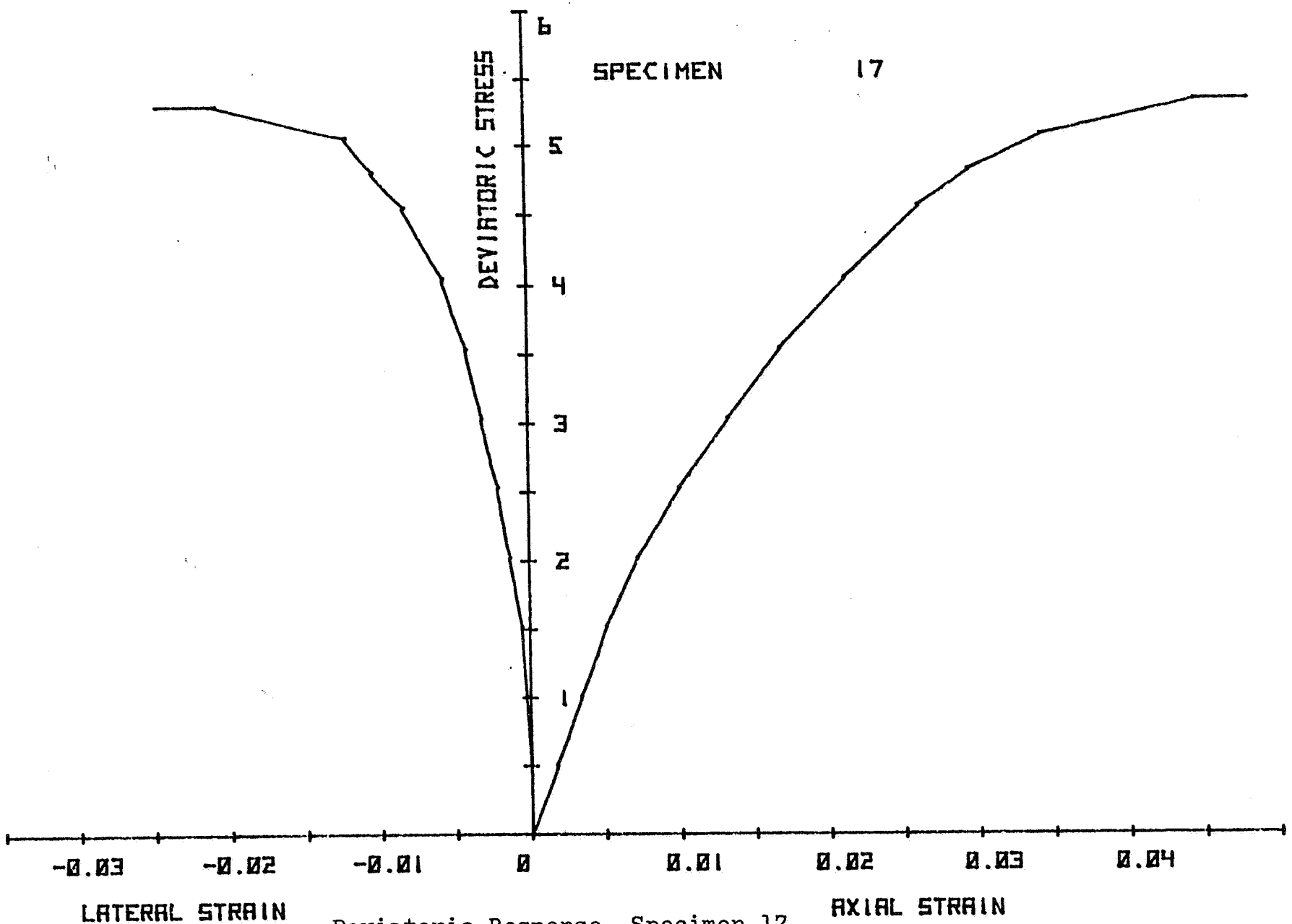

Deviatoric Response, Specimen 17
Figure 30

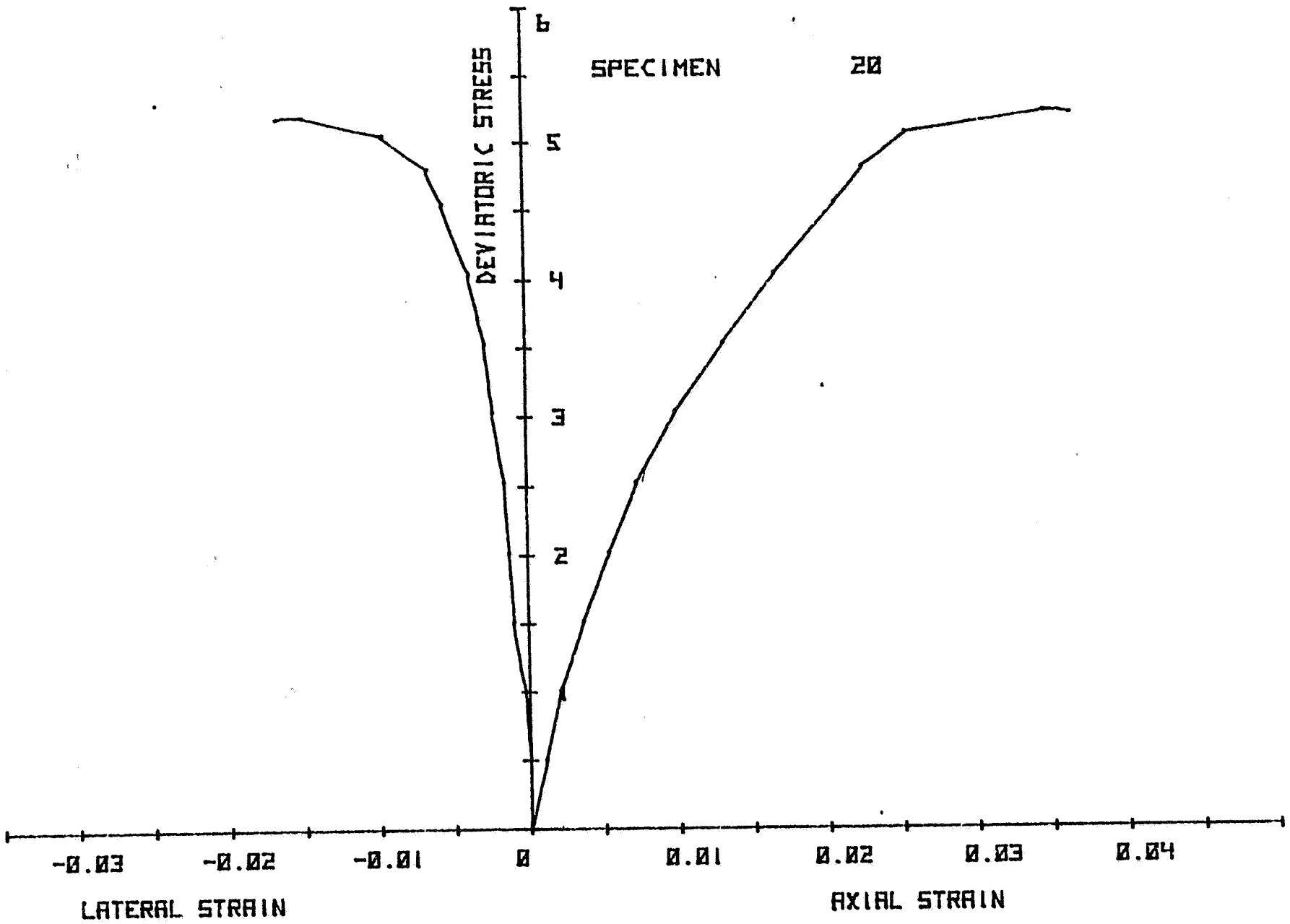

Deviatoric Response, Specimen 20
Figure 31

Atkinson-Noland & Associates, Inc.
Consulting Engineers

BY ..... DATE ..... SUBJECT ..... SHEET NO. ..... OF .....
CHKD. BY ..... DATE ..... JOB NO. .....

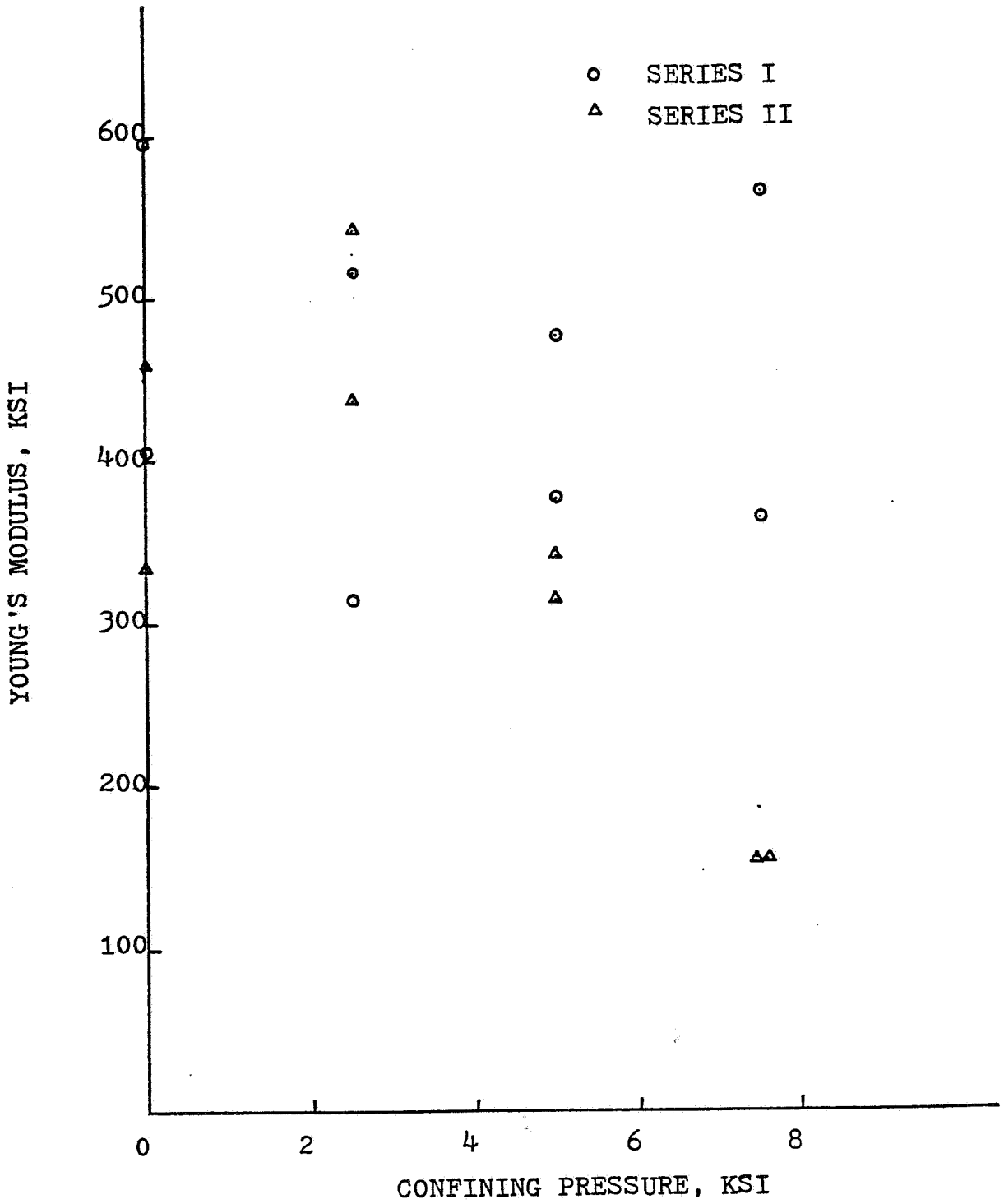

YOUNG'S MODULUS versus CONFINING PRESSURE

Figure 32

Atkinson-Noland & Associates, Inc.
Consulting Engineers

BY ..... DATE ..... SUBJECT ..... SHEET NO. ..... OF .....

CHKD. BY ..... DATE ..... JOB NO. .....

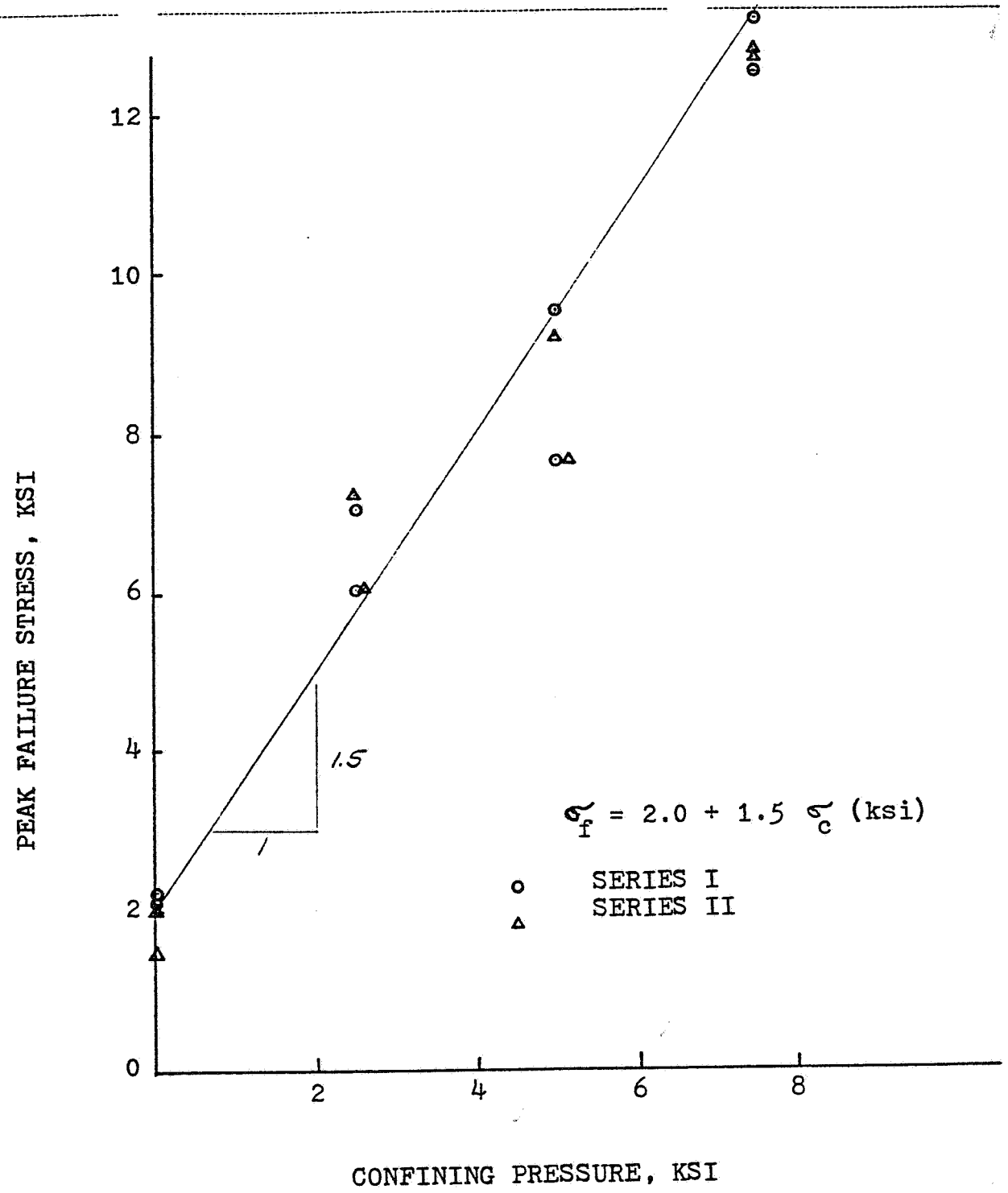

FAILURE STRESS versus CONFINING PRESSURE

Figure 34

APPENDIX B:

LATERAL INERTIA EFFECTS ON ROCK FAILURE IN SPLIT-HOPKINSON-BAR EXPERIMENTS

LATERAL INERTIA EFFECTS ON ROCK FAILURE IN SPLIT-HOPKINSON-BAR EXPERIMENTS

by C. Young and C.N. Powell,
Colorado State Univ.

This paper was presented at the 20th U.S.Symposium on Rock Mechanics, held in Austin, Texas, June 4-6, 1979. The material is subject to correction by the author. Permission to copy is restricted to an abstract of not more than 300 words. Write: Dr. Ken Gray, U. of Texas at Austin, Petroleum Engineering Dept.

ABSTRACT

Large increases in rock strength observed in split-Hopkinson-bar (SHB) experiments have often been attributed to a transition to more strongly rate dependent failure mechanisms. In more recent studies, it has been suggested that lateral inertia can play a significant role in the failure of rock in SHB tests. The electromagnetic gage method for measuring in-material particle velocities has been modified for use in SHB tests so as to provide a direct measure of radial particle velocities associated with sample failure. Experiments on samples of Westerly granite and Solenhofen limestone under a variety of SHB loading conditions demonstrate that sample failure does not occur homogeneously but, rather, begins at the exterior of the sample and propagates in a progressive fashion towards the axis of the sample. Integration with time of the particle and phase velocities at any point within the sample provides directly the cross-sectional volume of the sample at that point. Integration inward with radial distance of the material accelerations provides a measure of the radial stresses acting within the sample during failure. These radial stresses act as an effective confining pressure and can increase significantly the axial stresses at which failure takes place. The radial stresses induced, and the consequent increases in strength, can be coupled to the mode of failure. The granite undergoes a predominantly brittle, pressure sensitive mode of failure, wherein dilatancy requires large radial velocities, accelerations and stresses. The radial stresses act as confining stresses giving the rock significantly greater axial strength. In contrast, only moderate radial confining stresses in the limestone are required to induce predominantly ductile failure,with a concordant reduction in dilatancy and radial accelerations. The results illustrate that the traditional inferrence of high sample strength at SHB loading rates is due to the coupling between progressive sample failure and a Mohr-Coulomb failure surface and is not an intrinsic rate effect. While traditional SHB tests may thus be of limited value, properly instrumented SHB tests can provide much valuable data on high-rate sample failure and the relative importance of geometrical versus intrinsic rate effects.

References and illustrations at end of paper.

INTRODUCTION

The evaluation of novel drilling and rapid excavation techniques and the further optimization of conventional rock blasting both require an improved understanding of rock strength and failure characteristics at high rates of loading. As split-Hopkinson-bar (SHB) devices can provide rates of loading comparable to those of many rock breakage processes, they have been extensively used to deduce dynamic strengths for a large variety of rock types.

Using an SHB technique Green and Perkins (1968) found for strain rate increases from 10^2 to 10^4/sec. a sharp exponential increase in failure stress for Solenhofen limestone. Similar behavior was detected for porphyritic tonalite in the region of 10^3/sec. (Perkins et al., 1970). Perkins et al. (1970) have attributed these apparently anomalous strengths to a transition to a more strongly rate dependent failure mechanism. Using data from static triaxial compression tests Janach (1977) has predicted a failure strength for Westerly granite at high strain rates which suggests a very weak strain rate dependence. A question as to whether the state of stress was one of uniaxial stress or uniaxial strain at high strain rates was raised by Green and Perkins (1968). However, they attribute increases in failure strength at high strain rates to thermally activated fracture mechanisms. Brace and Jones (1971), and Janach (1976) interpret this behavior to be the result of a transition from uniaxial stress to uniaxial strain.

In more recent studies of rock failure at high strain rates, such as associated with SHB tests there has been a move to incorporate the effects of lateral inertia (Janach, 1976; Glenn and Janach, 1977). Janach (1976) developed a model (showing that lateral inertia could play a controlling role in SHB type rock failure and would be very important in the presence of dilatancy. Brace et al. (1966) have conducted triaxial compression tests at confining pressures up to 8kb, in which the amount of dilatancy, or inelastic volume changes, was found to be between .2 and 2 times the elastic volume change. This range in magnitude was found to be fairly independent of confining pressure. During dilatant behavior the porosity of a rock increases due to the formation of

predominantly axial fractures. Radial velocity records obtained during "symmetrical impact" experiments carried out by Glenn and Janach (1977), show a prolonged period of high radial acceleration, which they suggest is a direct result of dilatancy. Any permanent volume increases (dilatancy) will require, for conservation of mass, larger radial displacements and therefore velocities and accelerations. The higher radial acceleration will, through the conservation of momentum, require higher radial stresses which will act as an effective confining stress in the rock during failure. Brace and Jones (1971), and Janach (1976) suggest that the confining stress serves to maintain the axial core of the rock specimen in a state of uniaxial strain.

In the present study efforts have been concentrated upon the measurement of radial velocities in SHB tests, the calculation of radial stresses and volume changes and the quantitative evaluation of lateral inertia effects upon rock failure, including the contributions of dilatancy.

EXPERIMENTAL PROCEDURE

The modified split-Hopkinson-bar facility used in the experimental program is shown schematically in Fig. 1. The bar portion of the facility consists of a 2.4 m long aluminum H-channel, to which two sets of vertical supports have been secured. Cold-drawn, 304, stainless-steel bars 25.4 mm in dia. by 1.0 m long are suspended from the supports with 0.36 mm dia. stainless-steel (piano) wire. Support design details allow for adjustments in both the horizontal and vertical alignment of the suspended bars (Section X-X of Fig. 1). To insure precise bar alignment, an L-shaped plexi-glass block has been fastened to each of the vertical aluminum guide blocks. Each plexi-glass block is equipped with horizontal and vertical back-out screws. The proper position for each of these back-out screws was determined during alignment of the entire impact facility using a transit. Once alignment details had been insured, strain gage bridge circuits were epoxied to both the driver and receiver bars, to enable stress wave propagation within each bar to be monitored.

The unique feature of the facility is the Helmholtz arrangement of electromagnetic coils, shown schematically in Fig. 2. The field coils are aluminum spools wound with 14-gage Teflon-coated wire and are powered by three 12-volt automobile batteries connected in series. The coils are mounted on vertical supports located at the center of the 2.4 m H-channel, as shown in Fig. 2, and positioned so that the generated field is parallel to the longitudinal axis of the rock specimen. This gives a uniform magnetic field of approximately 0.05 Tesla in the region of the sample.

Dynamic fracture experiments were carried out on cylindrical specimens of Solenhofen limestone and Westerly granite. All rock specimens tested were 25.3 mm in dia., having lengths which varied between 46.0 and 51.2 mm. A standard diamond coring bit was used in conjunction with a variable speed drill press, to obtain cylindrical specimens from homogeneous blocks of the two rock types. Using a diamond saw, both ends of the rock specimen were cut perpendicular to the longitudinal axis of the rock core. The rock was then cut into two pieces of approximately equal length to allow for in-material gage placement.

Gage installation and rock specimen preparation consisted of three operations: the installation of in-material concentric gages, the reassemblage of rock halves, and the placement of an exterior circumferential gage. All gages were made of either varnished 32-gage copper wire or Teflon-coated 30-gage wire and carefully glued into machined concentric grooves with Locktite-404 adhesive (see detail in Fig. 2). Excess adhesive was removed from the rock face by hand-lapping against a 400-grit silicon carbide paper. This last step also insured that the gage wires were flush with the rock face. The gage-diameters, outlet gaps, and half-specimen lengths were then measured and recorded. Next, a thin layer of 5-minute epoxy was applied to the gage face and the two specimen halves reassembled. The performance of various circumferential gages was tested in the earlier stages of the research. The one found best for following the dynamic response of the two rock types tested, has a zig-zag configuration as shown in Fig. 2. This gage was prepared on a strip of cellophane tape using varnished copper 32-gage wire and then glued to the cylindrical rock surface in the vicinity of the epoxy glue joint, with Locktite-404.

During the SHB tests the voltage signals from the in-material and surface electromagnetic gages were recorded on Biomation model 805 transient digital recorders. The signals from the strain-gage bridge circuits on each bar were amplified through Tektronix AM-502 differential amplifiers and then recorded with an oscilloscope camera on a Tektronix 7603 scope. Velocity of the impact piston was determined by measuring the time interval for the piston to travel between a shorting pin (installed near the exit of the gas-gun barrel) and the driver bar. A 0.03 mm sheet of stainless shim-stock was attached to, but electrically isolated from, the impact end of the driver bar with a thin coat of fast-drying spray paint. Impact of the piston against the bar short-circuited the foil, thus stopping the time interval counter, and triggering the Biomation recorders and the oscilloscope. After each experiment the memory of the digital recorders was transformed to a high resolution analog display via an x-y recorder. For each experiment the magnetic field generated by the Helmholtz coils was monitored by recording a shunt voltage in the battery-coil circuit. This shunt voltage was calibrated with the magnetic field using a Hall effect probe.

DATA REDUCTION AND ANALYSIS

The basic experimental conditions and test results for the six experiments analyzed in detail are summarized in Table 1. The radial velocity gage reocrds for these six experiments were redigitized utilizing a Hewlett-Packard 9872-A plotter interfaced with an H-P 9825-A desk top computer. All subsequent data reduction and analyses were done with the 9825-A computer and the results plotted on the 9872-A (Figs. 3 to 10).

All of the analyses were based upon information contained in the radial velocity vs. time records. Representative plots of velocity vs. time are shown in Figs. 3 and 6. The exterior circumferential-gage has been designated as Gage #1, and the innermost in-material gage as Gage #3. Radial acceleration of any gage was determined from the slope of the appropriate velocity-time curve. An instantaneous value of gage radius was found by integrating the appropriate velocity-time curve.

Because of their inability to undergo large radial deformations the in-material gages failed relatively early as seen by the sharp discontinuities for Gages #2 and #3 in Figs. 3 and 6. In contrast, the circumferential gages had a zig-zag configuration, and were able to undergo quite large radial displacements before failure.

The early time, oscillatory portion of the gage records corresponds to the elastic response of the rock samples to stress waves propagating back and forth in the samples as they "rang" up to the input stress level of the driver bar. The negative velocity indicated for the first such motion in the granite samples (Fig. 6) may be due to an anomalously negative Poisson's ratio under SHB loading conditions or may be due to initial piezoelectric noise generated in the quartz-bearing rock. As soon as significant sample failure begins to occur all of the velocity records display the large regularly increasing signals shown in Figs. 3 and 6.

The variations in radial velocity over sample radius can be quantitatively described by the phase-velocity, C_u, where $C_u = (\partial h/\partial t)_u$, and where h is the Lagrange coordinate position. C_u is the velocity at which a given radial particle velocity is transmitted radially through the rock. As a means of determining the value of C_u at each of the initial gage locations and at all intermediate positions, velocity-time data for each gage has been transformed to t/h coordinate space and second-order polynomials used to connect points having the same radial particle velocities. Values of C_u were determined by taking the inverse-slope of the polynomial at each gage location, and were used in the integration to determine the cross-sectional volumes of the rocks during failure.

Finite-difference approximations to the equations for the conservation of mass and momentum (Fowles, 1970) were derived and utilized to calculate the cross-sectional volume (axial shortening is ignored) and radial stresses acting during SHB sample failure. The volume integration revealed that, for similar loading conditions, the granite samples underwent significantly greater cross-sectional volume increases than the limestone samples. This increased volume is attributed to the greater dilatancy occurring during failure of the granite samples. This increased volume has two important consequences on the analysis and interpretation of sample failure. Conservation of momentum requires that increased radial velocities and thus accelerations be associated with dilatant volume increases. Consequently, the radial stresses calculated for failing granite samples is much greater than for comparably loaded limestone samples. As tensile hoop stresses, developed as an SHB sample deforms radially, will contribute to the generation of radial compressive stresses, a sample not undergoing tensile failure will develop larger radial stresses. In the integration for calculating radial stresses, a criteria for tensile hoop failure was based upon the cross-sectional relative volume. As discussed in greater detail below, the large volume increases associated with failure of the granite specimens rapidly dictated that tensile hoop stresses could not be sustained.

The finite-difference equation for conservation of momentum was used to evaluate the effect of four different sets of assumed conditions upon calculated sample response. One condition related to the presence or absence of a hoop tensile strength during sample radial flow and failure. The other condition involved considering or ignoring the small changes in radius and density occurring with sample failure. Permutation of these two conditions made the four sets considered. It was found that inclusion of actual radii and densities had a negligible effect upon calculated radial stresses while inclusion of a tensile hoop strength could significantly increase the calculated radial stresses.

Evaluation of cases where tensile hoop stresses could contribute required a criterion for tensile failure. Although radial displacement and the consequent hoop strains would appear to be an adequate reference for tensile failure, large hoop strains could result from ductile flow without any concordant tensile failure. Consequently it was decided to utilize the cross-sectional relative volume ($\bar{V}$) as a reference for failure, on the basis that an increasing relative volume would be indicative of dilatant and, by inference, brittle failure. Quite arbitrarily a cross-sectional relative volume of 1.02 was employed as the cut off for the existence of a 200 bar tensile hoop strength. Despite the crudeness of the criterion, the results illustrate well the important role that hoop tensile strength effects can play.

As changes in radius and density had a negligible effect, only the effects of hoop tensile strength will be discussed here. In Fig. 4 radial stresses for the two tensile strength cases at different times are plotted as a function of position within the sample for the Solenhofen limestone test whose raw velocity data is shown in Fig. 3. At all three times shown, the cases in which a 200 bar tensile strength is included give a significantly higher radial stress. For all cases the radial stress is found to increase towards the axis of the sample as would be expected. Curves for the two cases at the latest time shown (93.8 μsec) are only slightly different as tensile failure has been generally invoked by the relative-volume criterion. The calculated loss of tensile strength during sample failure is illustrated in Fig. 5, where the radial stress at Gage #3 is seen at early times to be some three times greater for the tensile-hoop-strength case than for the zero-strength case. At later times the tensile-strength case radial stress rapidly approaches the zero-strength case.

In contrast to the limestone samples, Westerly granite samples displayed significantly higher accelerations and peak velocities such as shown in Fig. 6. The higher accelerations observed in granite samples are believed to be a direct consequence of dilatancy during brittle failure and the conservation of mass and momentum. As shown in Fig. 7 the radial stresses calculated for the velocity records of Fig. 6 are much larger than for limestone failure under comparable loading conditions.

The effect of including tensile rock strength with the relative-volume failure criterion on radial stress computations for Westerly granite is much less than for limestone. For Experiment 44, Fig. 8, the initial value of radial stress at the position of Gage #3 is only 20% greater than the corresponding value for the zero-tensile-strength case. The influence of tensile rock strength also became negligible at a comparatively earlier time than for the limestone experiments. The fact that the influence of tensile rock strength drops off rather abruptly for Experiment 44 indicates that the cross-sectional relative volume increases abruptly and that

the granite specimen has undergone a predominantly brittle and dilatant failure.

While the large differences in radial stresses generated by lateral inertia between limestone and granite are indicative of the different modes of failure for the two rocks, the radial stresses do not directly give the axial strength of the sample. As observed by a number of investigators (i.e. Mogi (1966); Brace et al. (1966); Byerlee (1967)) the relationship between the principal stresses σ_1 and σ_3 at failure is nonlinear. Byerlee (1967) suggests that the nonlinearity is due to the fact that the cohesive shear strength of rock (i.e. τ_o) varies with normal stress. Using triaxial compression data from Brace et al. (1966) and Mogi (1966), Janach (1977) was able to empirically establish a failure relationship for Westerly granite:

$$\sigma_1^2 = 1.05 \times 10^4 \ (\sigma_3+5)(MN/m^2).$$

This failure criterion when related to radial stress enables a determination of σ_1 (maximum axial stress) at failure. The general applicability of this model, as pointed out by Janach, is unknown. However, it has been found accurate in predicting the failure strength of Westerly granite at very high strain rates.

The radial stresses determined for each experiment on granite were used to determine an inferred axial strength as a function of radial position for Experiments 40 and 44. The inferred axial strengths from Janach's (1977) failure relationship for these two experiments are shown in Fig. 9. A lower bound for the inferred axial strength of Westerly granite was calculated using the frictional shear strength vs. normal stress data for this rock as presented by Byerlee (1967). The frictionally inferred axial strengths as a function of radial position for Experiments 40 and 44 have been included in Fig. 9.

Transmitted stress-wave amplitudes, as traditionally measured in SHB tests, provide a measure of the effective axial strength of the rock samples. In order to compare the inferred axial strengths (Figs. 9 and 10) deduced from the integrated radial stresses with transmitted wave amplitudes, an average sample strength was obtained by integrating the inferred axial-strength profiles over the radii (annular areas) of the samples. The maximum values for the average effective sample strengths so calculated are given in Table 1. The average strengths based upon Janach's (1977) rock fracture relationships are significantly higher than the measured transmitted stresses. The average strengths based upon rock friction data are comparable to the transmitted stresses except for SHOT #40.

For Solenhofen limestone a plot of σ_1 vs. σ_3 based upon the triaxial compression data of Robertson (1955) and Serdengecti and Boozer (1961) as presented by Handin et al. (1967), has been used to determine the inferred axial strength of the limestone as a function of radial position, for Experiments 33, 35, and 37. These curves are shown in Fig. 10. For Solenhofen limestone Janach (1976) has determined an upper limit for the peak axial stress that can develop in this rock under dynamic loading conditions. He has determined this dynamic limit to be between 1.3 and 1.4 times greater than the unconfined compressive strength. The average values of axial strength computed for Experiments 33, 35, and 37 and given in Table 1 lie within these dynamic strength limits. As f r as the tests on granite, the calculated strengths of limestone are more than adequate to explain the measured transmitted stresses.

CONCLUSIONS

Rock failure in split-Hopkinson-bar tests is strongly influenced by lateral inertia and the consequent generation of effective confining stresses. The electromagnetic-gage measurement of radial velocities at various radii in cylindrical split-Hopkinson-bar samples during sample failure permits the inertial effects to be quantitatively evaluated. Data on both Solenhofen limestone and Westerly granite illustrate the range of lateral inertia effects that occur in split-Hopkinson-bar tests. The principal conclusions that can be drawn from these data and their analyses are as follows:

1) Granite failure is characterized by high radial velocities, accelerations, and stresses.

2) Limestone failure is characterized by comparatively lower radial velocities, accelerations, and stresses.

3) For the tensile-strength criterion chosen, the effect of tensile rock strength was more pronounced in experiments where limestone was the rock tested. The effect of tensile rock strength drops off gradually for the limestone whereas for the granite the drop off takes place more abruptly.

4) The average inferred axial strength of granite increases significantly with increasing impact stress, whereas for the limestone there appears to be a limit for the dynamic strength.

5) The inertially induced radial stress field is capable of producing a confining pressure of sufficient magnitude to account for increases in compressive strength of magnitude observed in split-Hopkinson-bar experiments.

REFERENCES

Brace, W.F. and Jones, A.H., 1971, Comparison of Uniaxial Deformation in Shock and Static Loading of Three Rocks; J. of Geophysical Research, 76, 20, pp. 4913-4921.

Brace, W.F. Paulding, Jr., B.W., and Scholz, C., 1966, Dilatancy in the Fracture of Crystalline Rocks; J. of Geophysical Research, 71, 16, pp. 3939-3953.

Byerlee, J.D., 1967, Frictional Characteristics of Granite Under High Confining Pressure; Jnl. Geophys. Res., 72, 14, pp. 3639-3648.

Fowles, G.R., 1970, Conservation Relations for Spherical and Cylindircal Stress Waves; Jnl. Appl. Phys., 41, (6), pp. 2740-2741.

Glenn, L.A. and Janach, W., 1977, Failure of Granite Cylinders Under Impact Loading; Int. Journ. of Fracture, 13, 3, pp. 301-317.

Green, S.J. and Perkins, R.D., 1968, Uniaxial Compression Tests at Strain Rates from 10^{-4}/sec. on Three Geologic Materials; Final Report DASA-2199 and also Tenth Symposium on Rock Mechanics, Gray, K. (ed.), Austin, Texas.

Handin, J., Heard, H.C. and Magouirk, J.N., 1967, Effects of the Intermediate Principal Stress on the Failure of Limestone, Dolomite, and Glass at Different Temperatures and Strain Rates; Jnl. Geophys. Res., 72, (2), pp. 611-640.

Janach, W., 1976, The Role of Bulking in Brittle Failure of Rocks Under Rapid Compression; Int. J. Rock Mech. Min. Sci. & Geomech. Abstr., 13, pp. 177-186.

Janach, W., 1977, Failure of Granite Under Compression; Int. J. Rock Mech. Min. Sci. & Geomech. Abstr., 14, pp. 209-215.

Mogi, K., 1966, Some Precise Measurements of Fracture Strength of Rocks Under Uniform Compressive Stress; Rock Mech. Engng. Geol. 4, pp. 41-55.

Perkins, R.D., Green, S.J. and Friedman, M., 1970, Uniaxial Stress Behavior of Porphyritic Tonalite at Strain Rates to 10^3/second; Int. Jnl. Rock Mech. Min. Sci., 7, pp. 527-535.

FIGURE 1 LEGEND

1. Main H-Channel Support
2. Gas-Gun H-Channel Support
3. Gas-Gun Reservoir
4. Gas-Gun Barrel
5. Impact Bar
6. Receiver Bar
7. Bar Support-Yoke
8. Bar Guide-Block
9. Pneumatic Control Valves.
10. Rock Specimen
11. Helmholtz Coils
12. Strain-Gage Bridge
13. Electromagnetic Velocity Gage Leads
14. Compressed-Nitrogen Storage-Tank
15. Plexi-Glass Alignment Block
16. Shim-Stock Trigger
17. Impact Absorber
18. Time Interval Counter Trigger-Wire
19. Coil Support
20. Suspension Wire
21. Plastic Piston
22. Alignment Screws
23. Entry Port
24. Piston Valve-Seat
25. Gas-Gun Breech
26. Gas-Gun Alignment-Set-Screws

TABLE 1.

Principal Test Conditions and Results.

SHOT #	ROCK TARGET		IMPACT PROJECTILE		Input Stress Amplitude (kb)	Peak Trans-mitted Stress (kb)	Calculated Average Strength (kb)
	Rock Type	Length (mm)	Length (mm)	Velocity (m/s)			
33	Solenhofen limestone	46.8	199.5	32.1	5.94	2.9	3.5
35	Solenhofen limestone	46.0	199.5	41.7	7.72	2.9	3.4
37	Solenhofen limestone	51.0	99.5	61.4	11.36	2.9	3.6
40	Westerly granite	45.8	99.5	29.9	5.53	3.1	Fracture 4.3 / 2.4 Friction
42	Westerly granite	47.1	149.5	24.6	4.55	2.8	Fracture 5.2 / 2.7 Friction
44	Westerly granite	46.7	99.5	46.4	8.58	3.0	Fracture 6.3 / 3.3 Friction

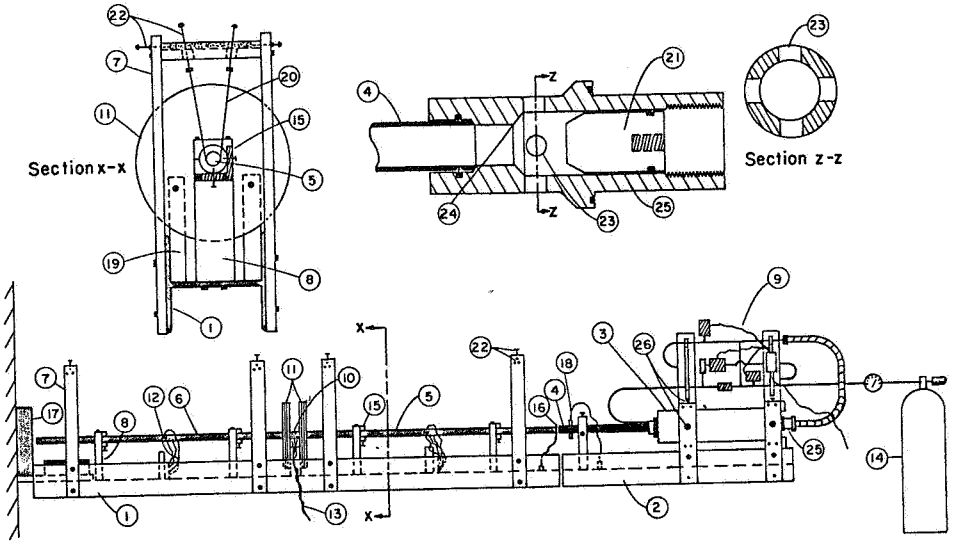

FIGURE 1 LEGEND

1. Main H-Channel Support
2. Gas-Gun H-Channel Support
3. Gas-Gun Reservoir
4. Gas-Gun Barrel
5. Impact Bar
6. Receiver Bar
7. Bar Support-Yoke
8. Bar Guide-Block
9. Pneumatic Control Valves
10. Rock Specimen
11. Helmholtz Coils
12. Strain-Gage Bridge
13. Electromagnetic Velocity Gage Leads
14. Compressed-Nitrogen Storage-Tank
15. Plexi-Glass Alignment Block
16. Shim-Stock Trigger
17. Impact Absorber
18. Time Interval Counter Trigger-Wire
19. Coil Support
20. Suspension Wire
21. Plastic Piston
22. Alignment Screws
23. Entry Port
24. Piston Valve-Seat
25. Gas-Gun Breech
26. Gas-Gun Alignment-Set-Screws

FIG. 1 - SCHEMATIC VIEW OF THE MODIFIED SPLIT-HOPKINSON-BAR IMPACT FACILITY.

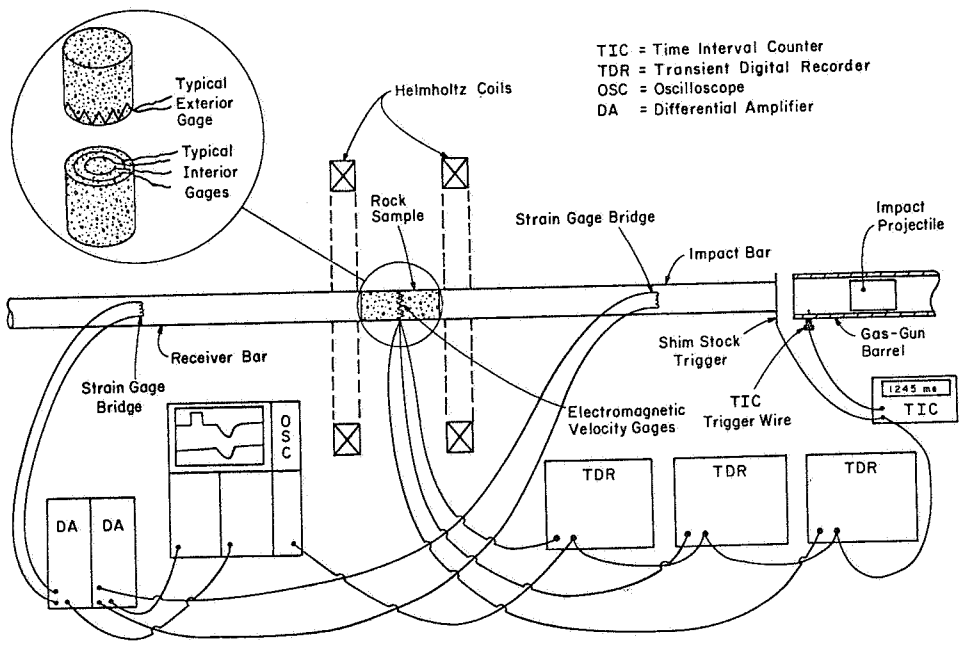

FIG. 2 - SCHEMATIC VIEW OF SHB SAMPLE INSTRUMENTATION AND DATA RECORDING.

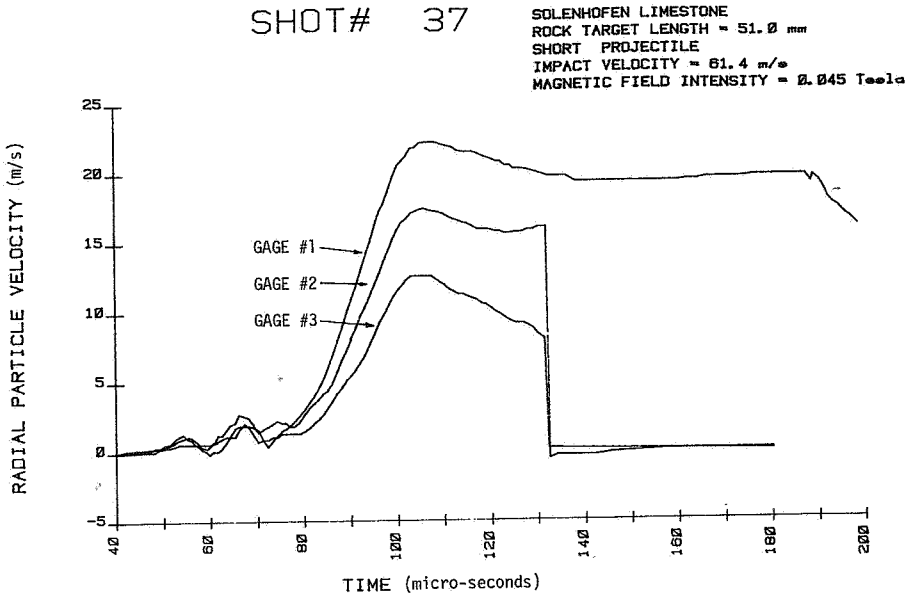

FIG. 3 - RADIAL PARTICLE VELOCITY VS TIME FOR SHOT #37 (SOLENHOFEN LIMESTONE). IMPACT STRESS AMPLITUDE = 11.36 KBAR; IMPACT STRESS DURATION - 50 μs.

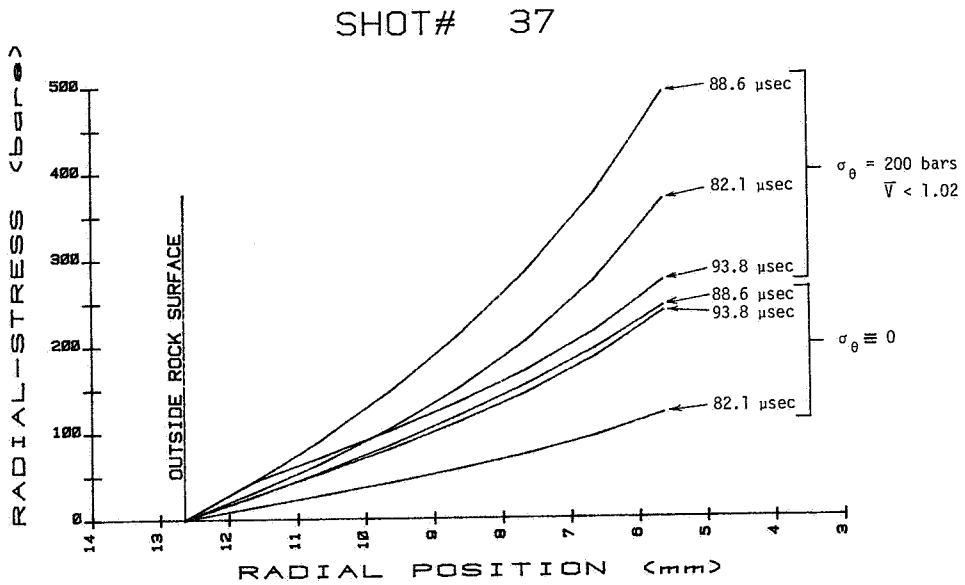

FIG. 4 - CALCULATED RADIAL STRESS VS RADIAL POSITION FOR SHOT #37 FOR TWO TENSILE STRENGTH CASES.

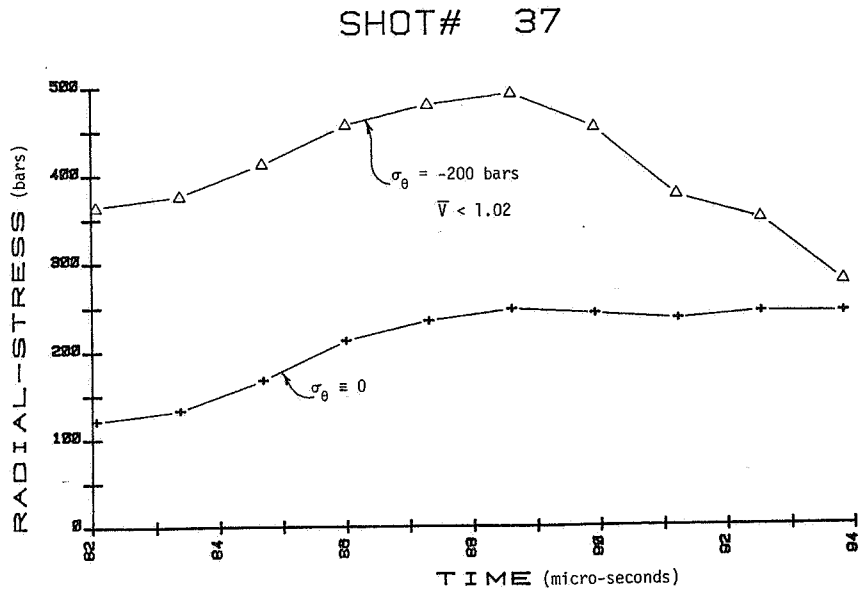

FIG. 5 - RADIAL STRESS (AT GAGE #3) VS TIME FOR SHOT #37 FOR TWO TENSILE STRENGTH CASES.

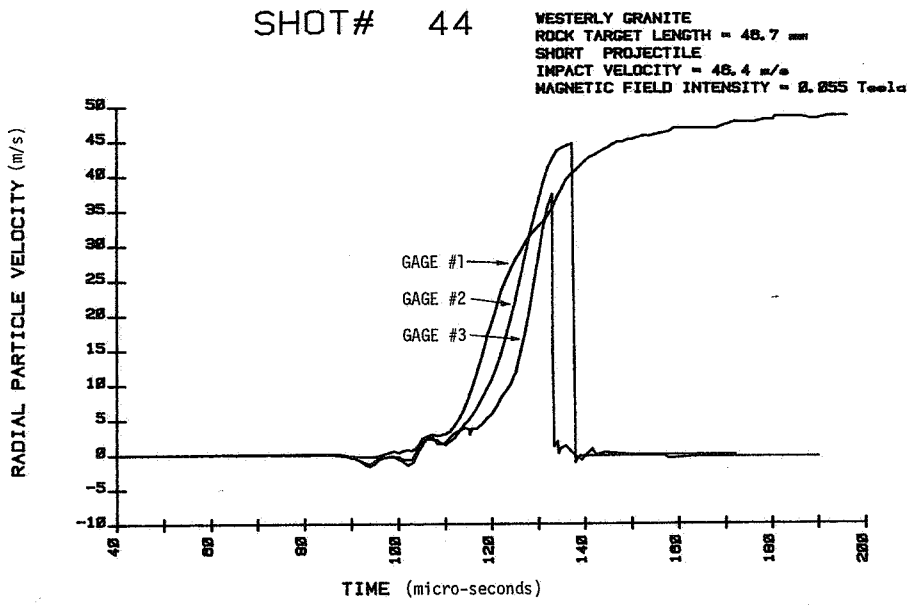

FIG. 6 - RADIAL PARTICLE VELOCITY VS TIME FOR SHOT #44 (WESTERLY GRANITE). IMPACT STRESS AMPLITUDE = 8.58 KBAR; IMPACT STRESS DURATION = 43 μs.

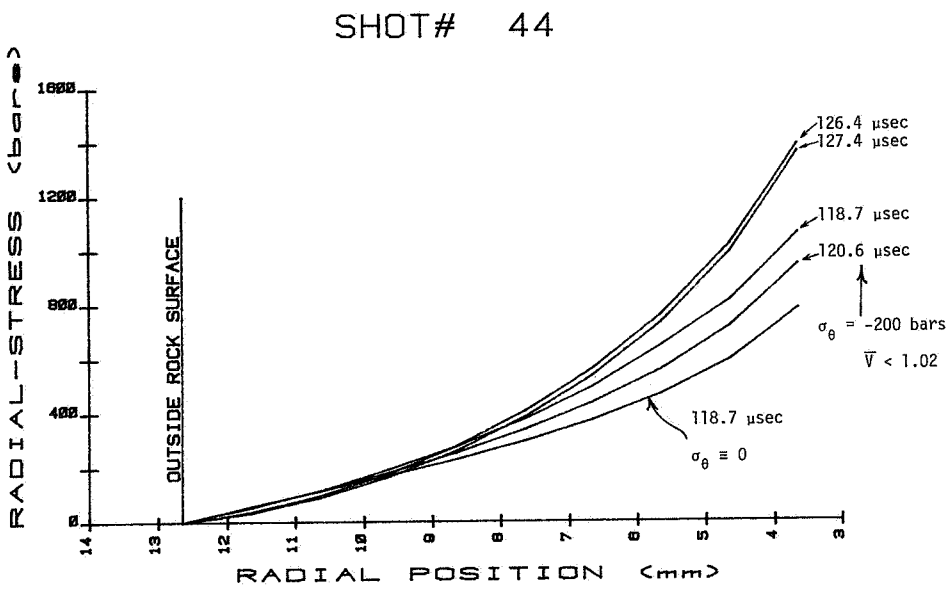

FIG. 7 - CALCULATED RADIAL STRESS VS RADIAL POSITION FOR SHOT #44.

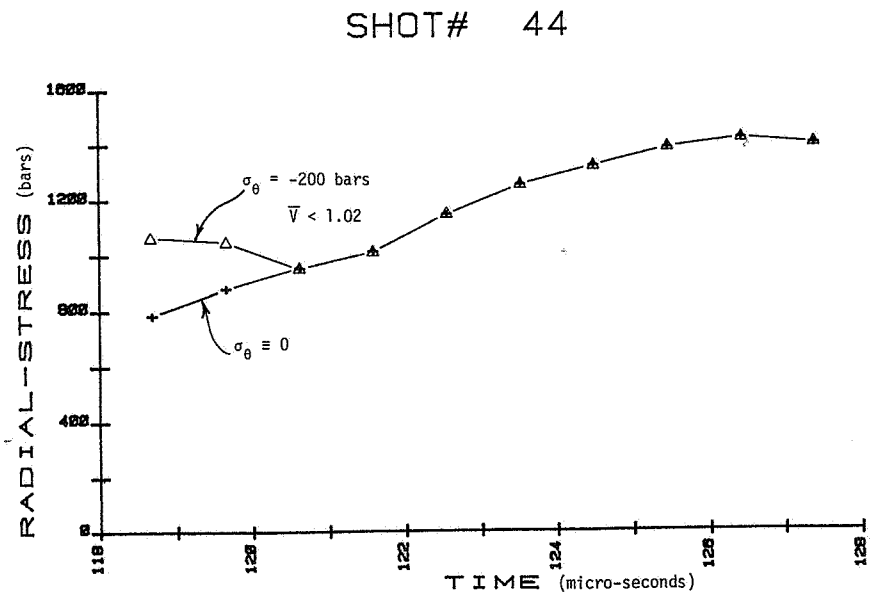

FIG. 8 - RADIAL STRESS (AT GAGE #3) VS TIME FOR SHOT #44 FOR TWO TENSILE STRENGTH CASES.

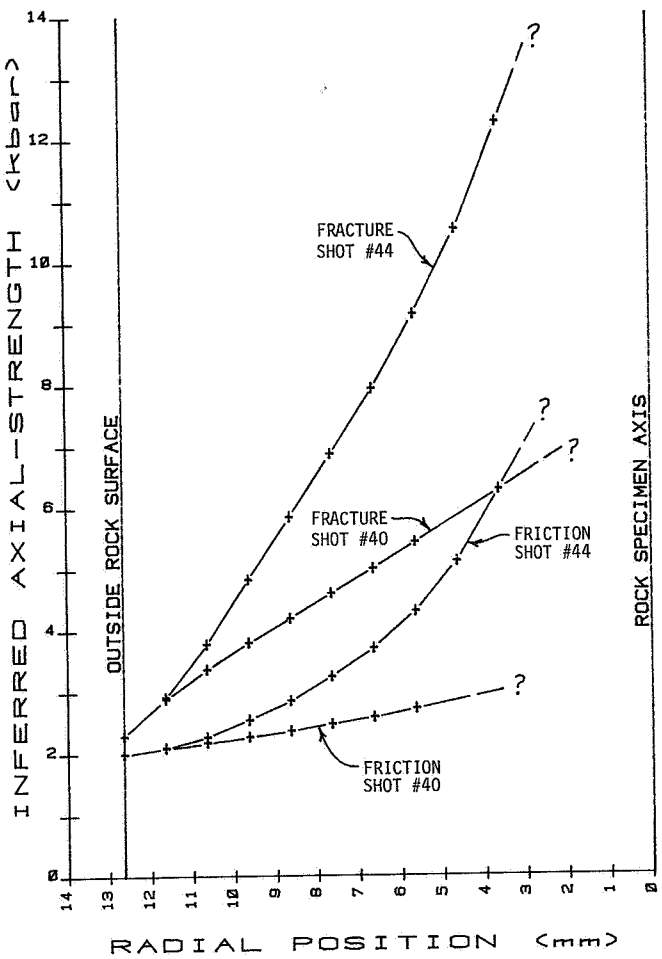

Fig. 9 - Inferred axial strength vs radial position for SHOT #40 and SHOT #44 on Westerly granite.

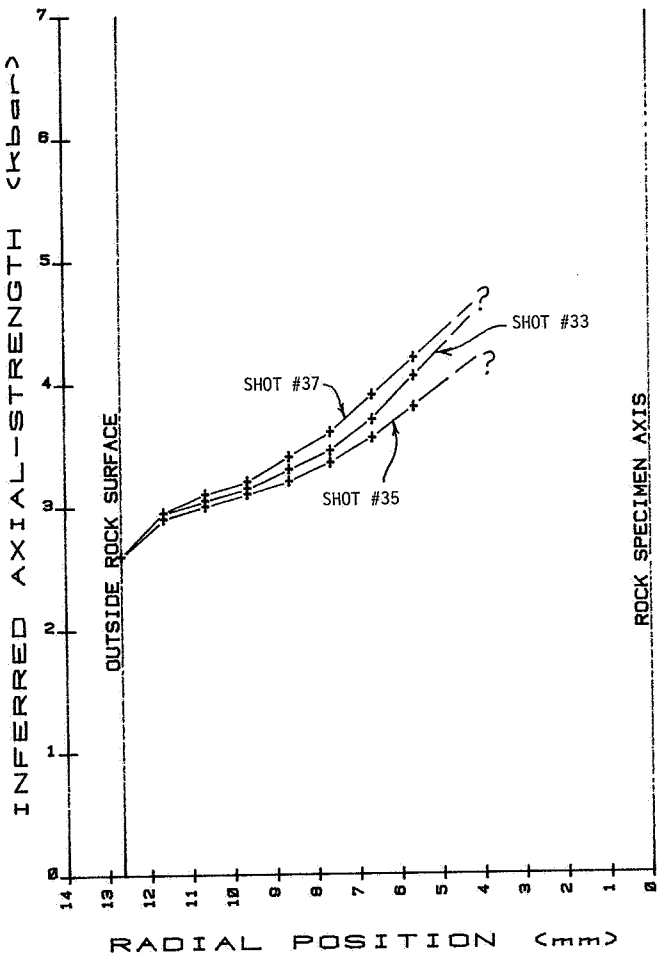

Fig. 10 - Inferred axial strength vs radial position for three tests on Solenhofen limestone.